Master Thesis

A Raman Study of CeO₂ Nanomaterials

with Different Morphologies

By

Meeseon Lee

Prepared at Fritz-Haber-Institut der Max-Planck Gesellschaft

November 2017

Supervisors:

Prof. Dr.-Ing. Habil. Delgado (FAU, Erlangen)

Dr. Annette Trunschke (FHI, Berlin)

Department of Chemical and Biological Engineering

Friedrich-Alexander University Erlangen-Nürnberg

Table of Contents

1   Introduction

1.1   General Properties of CeO$_2$

Cerium is the most abundant rare earth elements (66.5 ppm)[1] in the earth's crust. It can be found in various minerals including carbonate-fluorides and phosphates. Similar to the other lanthanide elements it occurs in oxidation state 3+, but also in 2+ or 4+ oxidation states.[2] Cerium 4+ is metastable in aqueous solution. The oxide could be easily oxidized at room temperature to form CeO$_2$ (ceria), the CeO$_2$ is the most common form of Ce in industrial application.

CeO$_2$ is a pale yellow-white powder with a chemical formula of CeO$_2$. But the oxide has to be rather considered as a nonstoichiometric oxide CeO$_{2-x}$, with $0 \leq x \leq 0.5$, while x primarily depends on the gas phase composition and the temperature. CeO$_2$ crystallizes in the fluorite structure with a face-centered cubic unit cell (F.C.C) within the space group Fm3m. In this stoichiometric structure, cerium cations are coordinated with eight equivalents nearest oxygen anions occupying the octahedral interstitial site; each oxygen anion is bonded to four cerium cations forming a tetrahedron. The fluorite structure is also stable after the loss of considerable amounts of oxygen, and the stoichiometric structure can be easily re-established in oxidizing atmosphere.[3] Oxygen defects and the corresponding Ce^{3+} cations are the major defects in CeO$_2$.
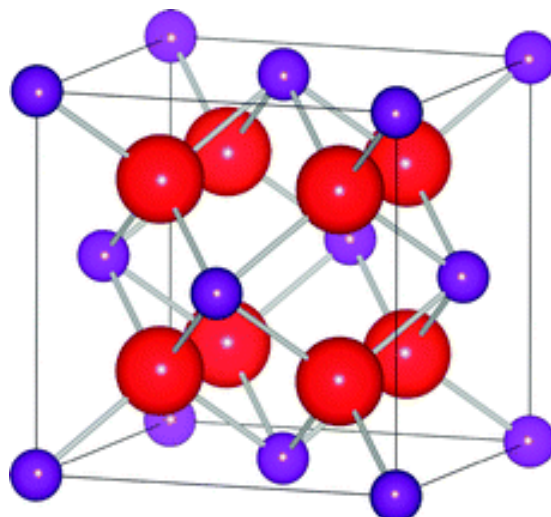
Figure 1. Structure of the stoichiometric CeO$_2$ with fourfold coordinated oxygen (represented by solid red balls) and eightfold coordinated cerium (represented by purple balls). Adopted from Malavasi, et al. [4]

The physical and chemical properties of cerium and CeO$_2$ have been attractive for decades and have been widely used in many fields such as glass-polishing agents[5] , alloys (iron, magnesium, and aluminum), in nanomedicine[6], phosphors[7], and catalysis. This versatile application could be attributed to the two stable valence states of CeO$_2$, cerium 3+ and cerium 4+, and its ability to change from one to the other depending on conditions coupled with the easy uptake and release of the oxide.[8] The change in the valence state of cerium can occur on the surface or in the bulk and can strongly modify the electronic and catalytic properties of the oxide. The formation of oxygen vacancies has been studied and apply its force field calculations.[9] According to the results oxygen vacancies on the surface are more stable than in the bulk.[10]

Oxygen defects can be classified as intrinsic and extrinsic defects, which are caused by thermal disorder or reactions between the solid and the surrounding atmosphere such as redox processes and impurities or foreign dopants, respectively.[11] As mentioned above, the most dominant and stable defects in CeO$_2$ are related to the presence of oxygen vacancies under a wide range of conditions. A reversible transition in the oxidation state of cerium ions from Ce^{4+} to Ce^{3+} may generate neutral oxygen vacancies in CeO$_2$. Gas phase O$_2$ (g) is formed if two oxygen ions (O^{2-}) leave the lattice, and the four electrons left behind were trapped and became localized at four cerium sites as shown in Figure 2.

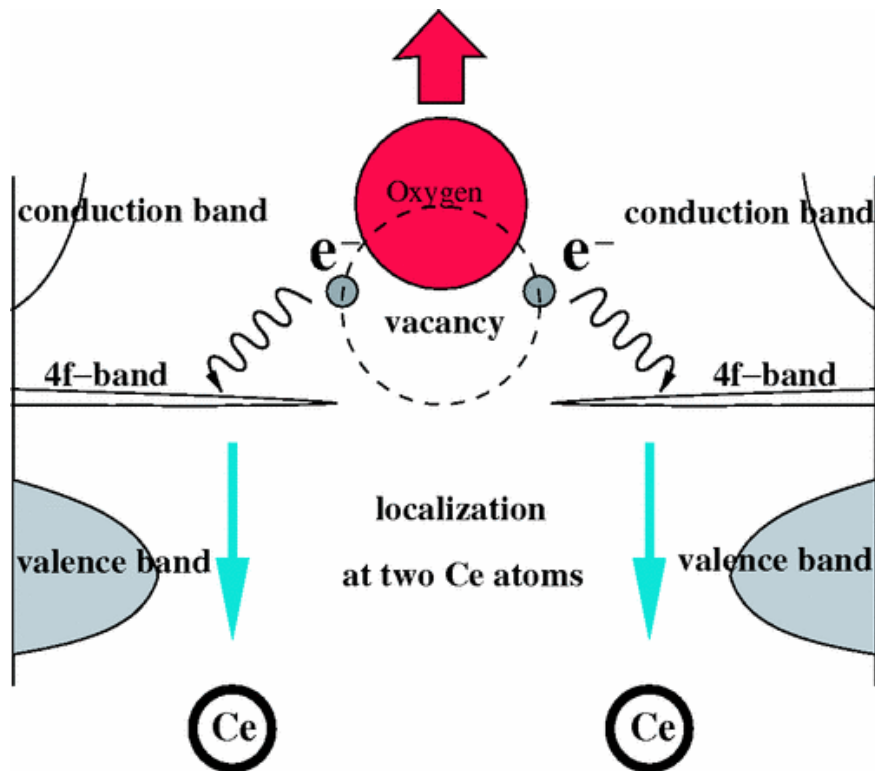**Figure 2. The process of oxygen-vacancy formation in CeO$_2$. An oxygen atom moves away from its lattice position leaving behind two electrons, which localize on two cerium atoms, turning Ce(4+) into Ce(3+). Adopted from Skorodumova, et al. [12]**

The property that CeO$_2$ easily releases and takes up oxygen make the oxide attractive for catalytic application in which oxygen transfer reactions are involved.[8b]

1.2   Catalysis

A catalyst accelerates a chemical reaction by opening new pathway with lower activation barrier without appearing in any of the products. The thermodynamic equilibrium of a chemical reaction is reached faster, but the position of the equilibrium is not changed. This ability is referred to as the activity of a catalyst, and selectivity is explained as selective promotion of one product out of multiple possible products. Catalysis is of major socio-economic importance for our society. In order to solve the future problems connected with limited resources and energy, as well as environmental protection, catalysis helps to develop green chemical processes: Replacing harmful and corrosive reagents, enabling more efficient processes, and reducing the environmental impact and coast of processes by avoiding waste formation. Catalysts are used in large-scale industrial processes such as oil refining, or polymer manufacturing, and future improvements of the activity and selectivity of the corresponding catalysts have a great economic and ecologic impact.[13] Even though all catalysts operated based on the same principles in terms of electronic and steric characteristics of the active center, catalysts in chemistry are usually classified into homogeneous and heterogeneous catalysts.[14] In the heterogeneous catalysis and reactants are in different phases, while in homogeneous catalysis catalyst and reactants are in the same phase. Most frequently homogeneous catalysts are liquid, whereas heterogeneous catalysts are often solid. Advantages and disadvantages as well as operation conditions are compared in Table 1.[15]

Table 1 . The advantages and disadvantages of homogeneous- and heterogeneous catalysis.[15]

	Homogeneous catalysis	Heterogeneous catalysis
Activity (relative to metal content)	High	Variable
Selectivity	High	Variable
Reaction conditions	Mild	Harsh
Service life of catalysts	Variable	Long
Sensitivity toward catalyst poisons	Low	High
Diffusion problems	None	High
Catalyst recycling	Expensive	Not necessary
Variability of steric and electronic properties of catalysts	Possible	Not possible
Mechanistic understanding	Plausible under random conditions	More or less impossible

The main advantage of using a heterogeneous catalyst is the relatively easy separation of the catalyst from the reactants and the products rendering continuous chemical processes possible. Also its tolerance to extreme operation conditions is higher compared to homogeneous catalysts. Most of the large scale industrial processes are performed in presence of heterogeneous catalysts, such as the system or ammonia from the elements by the Haber-Bosch process (Fe) for production of fertilizers and explosives, methanol synthesis ($Cu/ZnO/Al_2O_3$), Fischer-Tropsch synthesis (Co, Fe) for production of synthetic fuels, and cracking and alkylation (Zeolites, Clays, Silicates) for production of high-octane fuels.[16]

A heterogeneous catalytic reaction consists of 3 steps; adsorption of reactants from the gas or liquid phase onto the catalyst surface, surface reaction of adsorbed species, and desorption of products into the gas or liquid phase. Therefore, the interface between the two phases (gas-solid or liquid-solid) is very important and requires fundamental studies aimed at a description of the chemical bonds between a catalyst surface and a molecule that is converted in a heterogeneously catalyzed reaction.[17]

1.3   Catalysis by CeO$_2$ and nanostructures

In heterogeneous catalysis different types of catalysts are used, including metal or oxide nanoparticles supported on carriers, like oxides, polymers or carbon materials, or bulk catalysts, such as alloys or oxides.[18]

CeO_2 has been widely applied due to its acid-base and redox properties as active phase itself or as support for metal or oxide nanoparticles. The most prominent application of CeO_2 is as a component of the automotive three-way catalyst (TWC) to reduce the emissions of gas engines[19].[19] Furthermore, cerium oxide has been considered in fluid-cracking catalysts (FCC), oxidation catalysts (e.g., low temperature CO and volatile organic compounds (VOCs) oxidation, and soot removal from diesel engine exhausts), or hydrocarbon reforming catalysts (e.g., partial oxidation, steam reforming, and water-gas shift).[20] Most applications are associated with the high oxygen storage capability, which makes rapid redox cycles

possible at low oxygen partial pressures and elevated temperatures leading to a mixed ionic electronic conductivity of ceria under reaction conditions. Due to the corresponding redox reactions, the oxidation states of cerium in CeO_2 varies under reaction conditions between Ce^{3+} and Ce^{4+}.[3] The varying oxidation state of cerium goes along with the concentration of oxygen vacancies on the surface and in the bulk of CeO_2.

Since heterogeneous catalysis occurs on the interface, heterogeneous catalysts are in most of the cases nanostructured materials, because nano-structuring increases the specific surface area and therefore the interface and consequently the efficiency of the catalyzed process.[21] When CeO_2 particles are turned into nano-sized particles, the surface area to volume ratio increases and the defect formation is changed resulting in CeO_2 with unique features in general. The defect formation energy can be remarkably reduced in nanostructured oxide with an increase in the level of nonstoichiometry. Furthermore, electronic properties such as the band gap, and magnetic moments, as well as specific heats of phase transformations, melting points, and surface structures are changed com,pared to bulk materials and layer nanoscales leading to high activities in energetically challenging reactions, high selectivity to valuable products and extended life times of catalysts.[22]

Recently, morphology engineering of catalyst nanoparticles appeared to be a successful strategy to tailor catalytic performance without affecting catalyst composition. In addition, well-defined particle morphologies facilitate the establishment of structure-performance relations. Based on previous studies, it was established that the redox property of CeO_2 strongly depends on different exposed facets on the surface of the nanocrystallites. The formation of oxygen vacancies on CeO_2 is considerably surface sensitive due to the different oxygen anion and cerium cation environments on the different surface terminations.[9] Generally three low-index lattice planes exist on the surface of CeO_2 nanocrystals: (100), (110), and (111) as shown in Figure 3. Other surfaces such as (211), (211), and (310) are less stable and would undergo severe reconstruction.[9, 23]
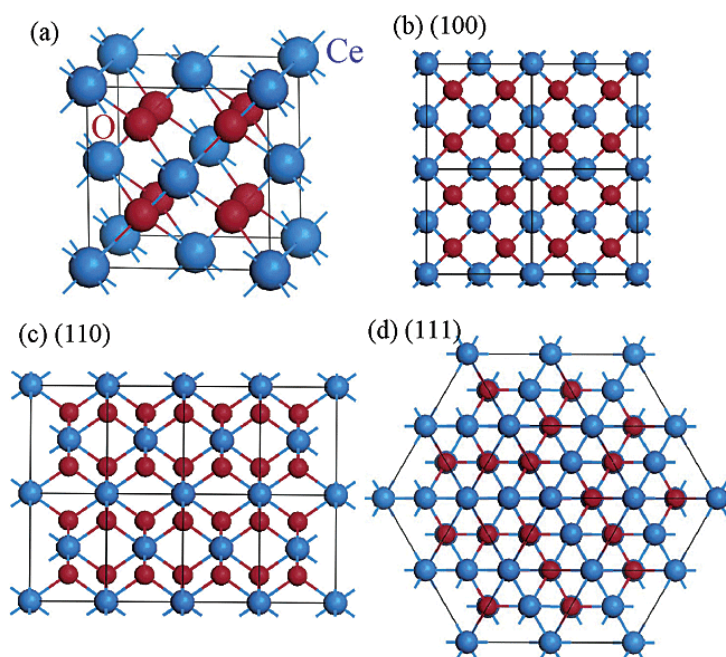
Figure 3. (a) Unit cell of the CeO₂ structure. (b) The (100) [(200)], (c) the (110), and (d) the (111) planes of the CeO₂ structure. Adopted from Wang and Feng [24].

The (100) planes have an unbalanced dipole because of the alternate arrangement of oxygen and cerium ions at the surface, which leads the facile migration of lattice oxygen. The (110) planes are also nonpolar due to the stoichiometric proportions of anions (three-folded oxygen) and cations (six-folded cerium), which leads to a zero dipole moment perpendicular to the surface. The (111) surface is terminated by threefold-coordinated oxygen atoms and sevenfold-coordinated cerium atoms, and it is also a nonpolar surface due to a neutral repeated three-plane units causing no net dipole moment. [25]

Calculations of the interionic potentials based on the Born model indicate that the formation energy of an oxygen vacancy is closely related to the surface structure and it is lower for the (110) surfaces than for the (111) surface.[26] Given the fact that the (111) facet has the highest oxygen vacancy formation energy due to the lower surface energies and structures of the pure surface, [27] the general consensus is that stability of these three facets follows the trend (111) > (100) > (110).[9, 28] In the case of CO oxidation, strong morphology effects were observed, which can be correlated to the morphology dependent reducibility and oxygen vacancy structures/concentrations.[25a, 29] But recently, another interesting work reported an opposite facet sensitivity of CeO₂ nanoparticles in oxidation on the on hand and hydrogenation catalysis on the other hand, in which the (100) surface predominantly

enclosed in CeO_2 nanocubes is optimal for the CO oxidation reaction, wherease the (111) surface most abundant in conventional polyhedral CeO_2 particles is responsible for selective hydrogenation reaction of C_2H_2.[30]

Thus CeO_2 with different morphologies possess different catalytic properties due to different surface properties as a result of the corresponding exposed facets. Nano-sized CeO_2 has been most frequently studied applying surface science techniques and investigating single crystals. In surface science the surface sites are characterized with every precision at the atomic scale. The corresponding preparation techniques produce stable surfaces with controlled termination and chemical composition allowing the investigation of the adsorption of reactants. However, single crystals seldom show functional properties due to the low surface area and the absence of defects. Well-defined polycrystalline powders exhibit high specific surface areas and consequently reactivity. Rod and cube-like morphologies can be easily synthesized by controlling several critical parameters such as pH, temperature, and pressure. Nanorods, which possess mainly (110) and (100) surface facets, and nanocubes, which expose mainly (100) facets, exhibit higher activity in CO oxidation and soot combustion reaction than CeO_2 with octahedral particles, which predominately expose (111) facets with the lowest surface energy.[31]

The purpose of the present study is to investigate the oxygen adsorption and activation (reduction) on the surface of polycrystalline ceria with well-defined particle morphology. Three morphologies will be included in the investigation: (i) a sample with less defined morphology (particles), and samples containing (ii) rod- and (iii) cube-like particles. Oxygen adsorption is studies by Raman spectroscopy coupled with gas chromatography (GC) and mass spectroscopy to analyze the products or CO and propane oxidation reactivity of adsorbed oxygen species.

2   Experimental Method and Setup

2.1   Preparation and characterization of CeO_2 samples

Nanostructured CeO_2 materials have been synthesized applying many different methods including chemical precipitation, hydrothermal/solvothermal synthesis and post-treatment, sol-gel techniques, sonochemical synthesis, microemulsion techniques, and methods using various templates.[32]

The nanostructured CeO_2 catalysts analyzed in the present study (particle, cube, rod) were provided by Dr. Teng Fu at the Fritz-Haber-Institut. CeO_2 nanocubes and nanorods were synthesized via a hydrothermal approach (Figure 4), and the particle sample was prepared by precipitation.
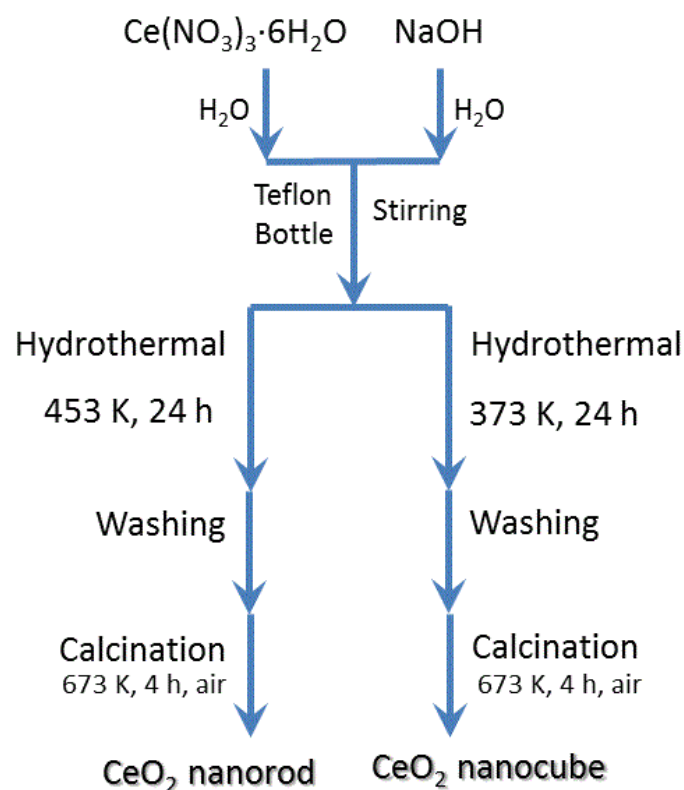

Figure 4. Synthesis procedure of nanostructured CeO2 rods and cubes via hydrothermal approach.

The precipitation method is an attractive synthesizes route due to the simple process, economic salt precursors and easy scale-up. In the present study, 7.5 g $Ce(NO_3)_3 \cdot 6H_2O$ were dissolved in 100 mL H_2O while the pH was adjusted to 10 by adding ammonium hydroxide solution. After aging at RT for 24 hours, the product was centrifuged and washed with water and ethanol, and then dried at 383 K for 3 h. The product was calcined at 673 K for 4 h (2K/min).

In contrast to precipitation at normal pressure, hydrothermal processing allows the synthesis of nanoparticles with different particle size and morphology. The pH of the reaction medium is considered as a significant parameter having an effect on the shape and crystallinity of the nanoparticles.[33] In our hydrothermal synthesis, 0.868 g of $Ce(NO_3)_3 \cdot 6H_2O$ dissolved in 5 mL of H_2O and 9.6 g of NaOH dissolved in 35 mL of H_2O were mixed in a Teflon bottle, and stirred for 30 min. The Teflon bottle was sealed in the autoclave and heated to 373 K. The hydrothermal treatment lasted for 24 hours, and then the product was centrifuged and washed with H_2O and ethanol. After drying at 333 K overnight, the product was calcined at 673 K for 4 hours (Figure 4).

In the present Raman investigation, CeO_2 with differently exposed crystal planes, which may lead to different surface stability, oxygen vacancy formation energy, and interaction with surface molecules, will be compared[34]. Morphology and phase composition of the CeO_2 samples prepared applying different synthesis techniques were characterized by Scanning Electron Microscopy (SEM), and Powder X-Ray Diffraction (PXRD) in advance.

SEM uses electrons rather than visible light like conventional light microscopes to generate structure images. The image generation of SEM is by the interaction between the incident electron beam and the specimen including different kind of scattered, adsorbed, or transmitted electrons as illustrated in Figure 5.[35]
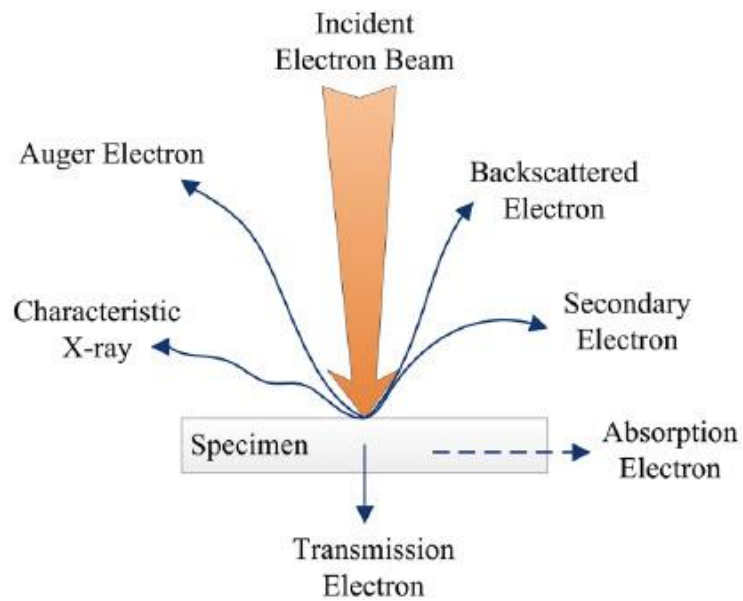
Figure 5. Generation of electron signals emitted by the interaction between the incident electron beam and the specimen surface. Adopted from Zhu, et al. [35] Copyright 2013 IEEE.

There are two main kinds of detection principles for morphology imaging: secondary electron (SEs) and backscattered electrons (BSEs). SE is usually preferred due to its very high resolution for morphology by topographies with an optimal signal-to-noise ratio. Compared to SE, BSE has too low resolution to characterize morphology, and the generation of BSE is more related to chemical elements.[36]

The micrographs of the different samples are shown in Figure 6. The different morphologies of CeO$_2$ were confirmed by the SEM images, showing irregular shaped particles for the "particle" sample and the expected cube- and rod-like morphologies, respectively, for the hydrothermally prepared samples. The mean size of the particles is 10.60 nm, and 9.45 nm for nanorods. For nanocubes, it varies in range of 10.34 - 36.25 nm.
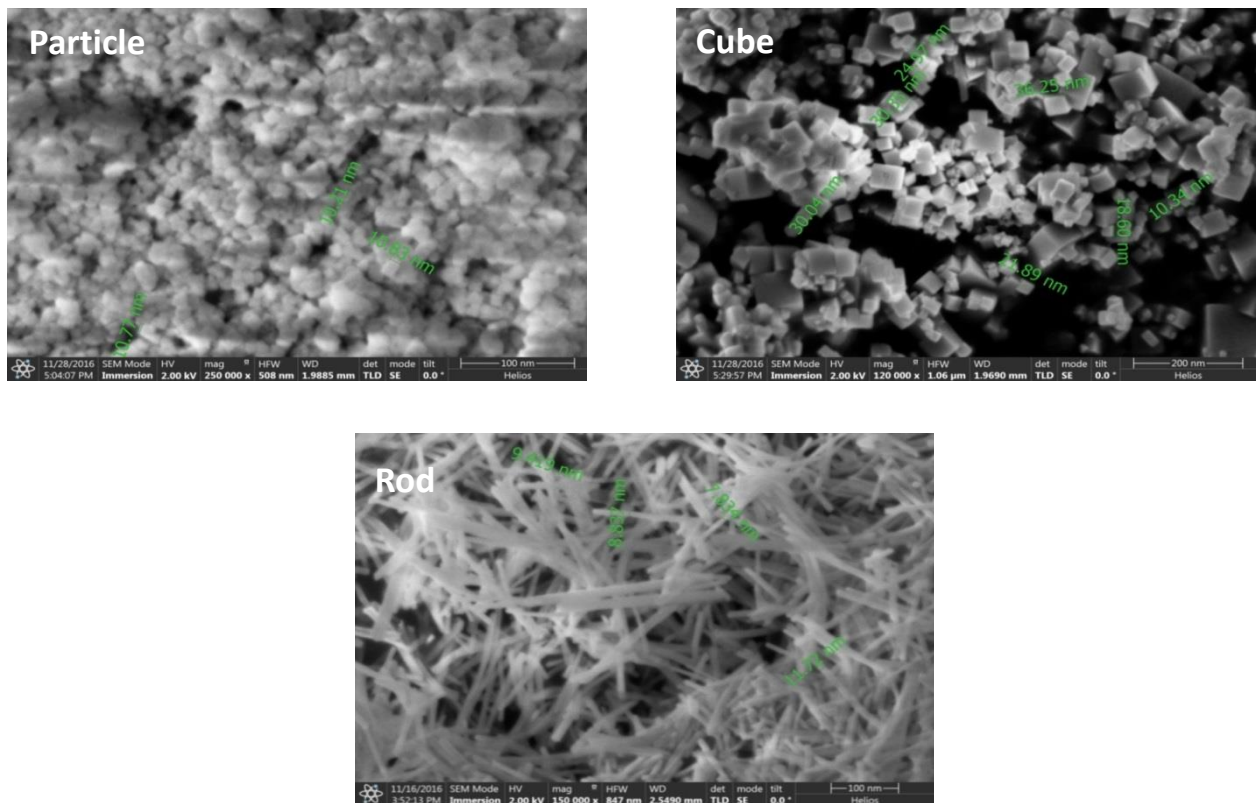
Figure 6. Morphology of particle, cube, and rod samples analyzed by SEM.

The phase purity of three morphologically differ CeO2 samples was analyzed by XRD. In XRD chart, a diffraction peak position is identical for same chemical compositions and physical properties. But an intensity of each peak is dependent on total area of each crystal face.
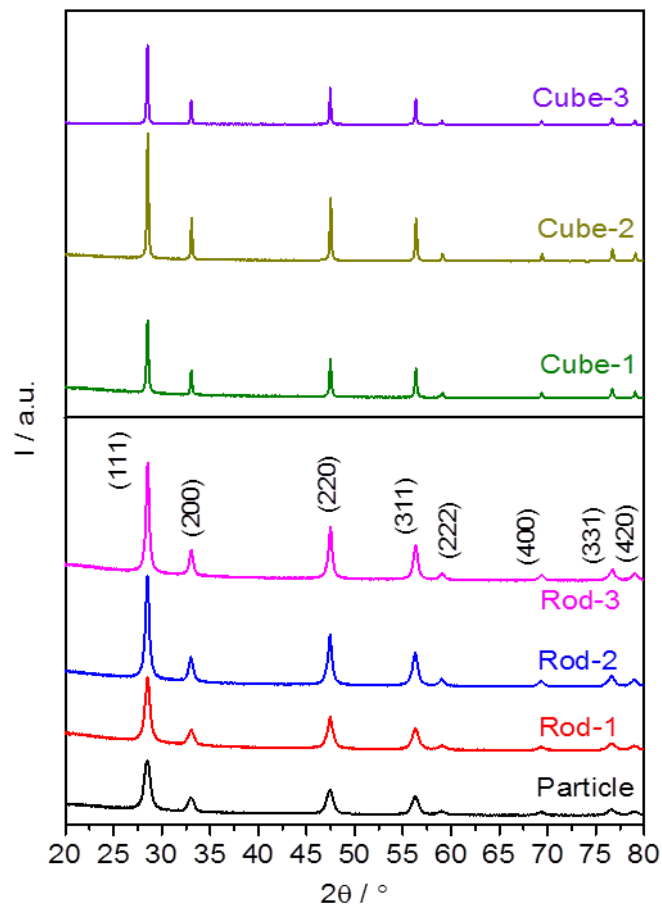
Figure 7. X-ray diffraction (XRD) patterns of the synthesized CeO$_2$ samples. Particle, Rod-1, and Cube-1 will be used in this present study.

The XRD patterns of synthesized CeO$_2$ nanoparticles are shown in Figure 7. The XRD profile confirmed the phase-purity of the polycrystalline CeO$_2$ samples. The high-intensity peaks are observed at 28.53, 33.09, 47.5, 56.26, corresponding to the 111, 200, 220, 311 crystal planes. No other diffraction peaks are detected indicating the pure cubic fluorite structure (JCPDS No: 34-0394). Differences in the intensity ratio of the different peaks are in accordance with the different morphologies of the three samples.

The specific surface area (S_{BET}) was determined by nitrogen adsorption at 77K and analysis of the adsorption isotherm in the $p/p_0 = 0.05–0.15$ pressure range assuming the N_2 cross sectional area of 16.2 Å^2 and using the method by Bruner, Emmett and Teller (BET). The BET surface areas of cubes, rods, and particles used in this study are measured to be 27.3, 89.3, and 83.5 m^2/g respectively as shown in Table 2.

Table 2. Sample information and BET surface areas of the different cerium oxides studied by Raman spectroscopy in the present work.

Sample	Sample Number	c(NaOH)/T$_{synthesis}$	S_{BET} (m^2/g)
Particle	25585	NH$_3$/293K	83.5
Nanorod	25694	6M/453K	89.3
Nanocube	25783	6M/373K	27.3

2.2   *(In situ)* Raman Spectroscopy

When monochromatic light interacts with molecules, the light may be absorbed, elastically or inelastically scattered. When the scattered light has same energy as the incident frequency, the process is called Rayleigh scattering. But if certain discrete frequencies above and below of the incident beam are observed in the scattered light, the process is referred to as Raman scattering or Raman effect. The change in frequency (wavelength) of the scattered photon provides chemical and structural information (Figure 8).
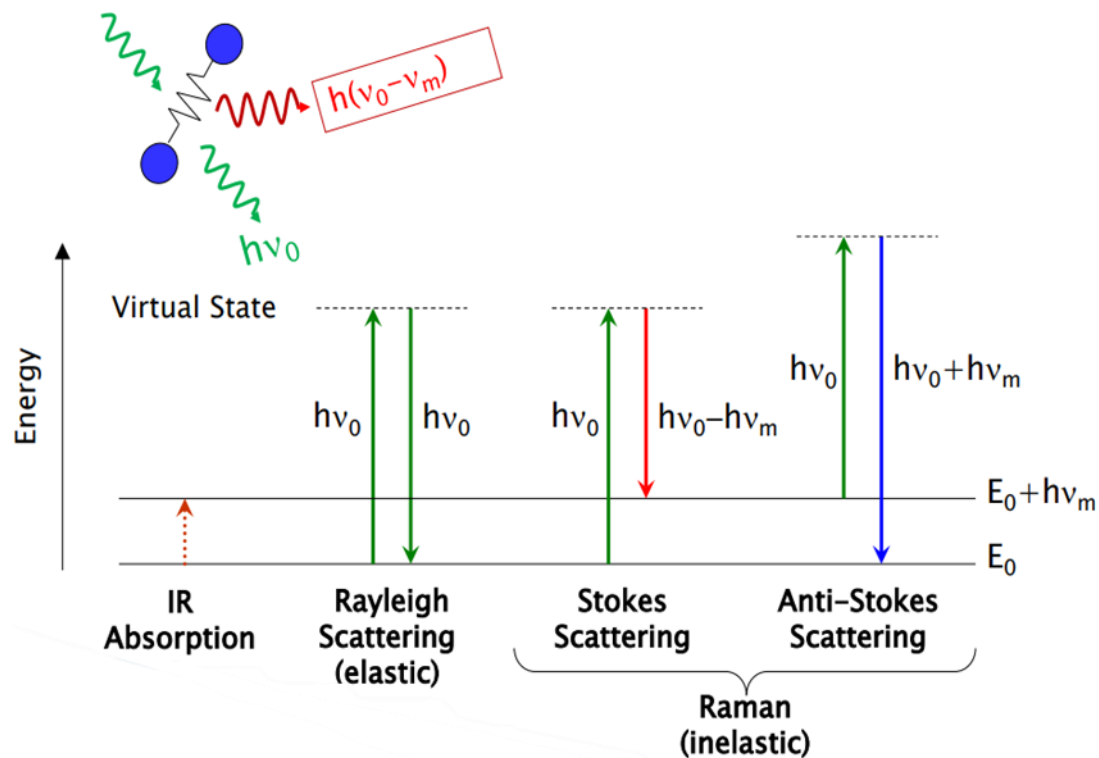
Figure 8. Schematic diagram of the energy transition involved in Rayleigh scattering and Raman scattering. Raman scattering occurs through the interaction of an incident photon with a molecular vibration mode, gaining(Anti-stokes) or losing(Stokes) an amount of energy equal to that vibrational mode.

Raman spectroscopy is based on the Raman-effect. It is a spectroscopic technique to study vibrational modes in a system. Since vibrational information is very specific for the chemical bonds in molecules, it therefore provides a fingerprint by assessing molecular motion. The

Raman scattered light occurs at wavelengths that are shifted from the wavelength of the incident light by the energies of molecular vibrations. Since it is governed by the polarizability of the electron cloud around the molecules, only vibrations in which the polarizability is changed are Raman active and vibrational modes that are more polarizable are more intense in the Raman spectrum.[37]

The Raman spectroscopy belongs to the handful catalyst characterization techniques, which are capable of providing structural level information concerning heterogeneous catalysts under controlled conditions (temperature, partial pressures of the gas phase components, etc.). Raman spectroscopy is not specifically surface sensitive, but rather a bulk technique. However, surface information is included in the measured spectrum. Raman spectroscopy provides, (1) bulk structural information, which can be used to follow (2) structural transformations of bulk and surface phases, and (3) can detect surface reaction intermediates. Raman spectroscopy was intensively used to study surface metal oxide species during oxidation reactions.[38]

In this study, *in situ* Raman spectroscopy was employed as a main instrument to detect adsorbed oxygen species on the CeO_2 surface and to investigate their reactivity with CO and propane. The aim was to monitor and determine the chemical transformation happening on CeO_2 during the reactions of adsorbed oxygen with reaction partners from the gas phase to help to understand the morphology-dependent properties of CeO_2 nanomaterials in CO and propane oxidation. Especially the characterization of superoxo (O_2^-) and peroxo (O_2^{2-}) species can be carried out by Raman spectroscopy. The weakening of the O = O bond in molecular oxygen by reduction of adsorbed oxygen to superoxide and peroxide can be followed by the shift in the frequency of the O-O stretching vibration.[39] The reaction products between adsorbed oxygen species and CO or propane, respectively, will be determined by micro GC.

2.3   Experimental setup

The experimental setup of Raman spectroscopy consisted of a triple-spectrograph system from Princeton Instruments with three stages. As shown in Figure 9, for excitation there were 532 nm, 457 nm and 355 nm single frequency continuous-wave diode-pumped lasers from Cobolt, a 488 nm laser (Sapphire SF) from Coherent, 442 nm and 325 nm He-Cd lasers from Kommon Koha, and a 266 nm laser (FQCW 266) from CryLaS. Gratings including 600 g/mm, 2400 g/mm and 3600 g/mm are used in the case of using visible (532 nm – 442 nm) and UV lasers (355 nm to 266 nm) excitations. Gratings including 150 g/mm, 300 g/mm and 1200 g/mm are used in the case of near infrared (NIR, 633 nm and 785 nm) and visible lasers excitations. Scattered light signals are monitored by back-illuminated CCD detectors (PyLoN:2K and PyLoN:100 from Princeton Instruments). The output of the laser will be maintained below 0.2mW for VIS, and 0.8mW for UV in all performed experiments.
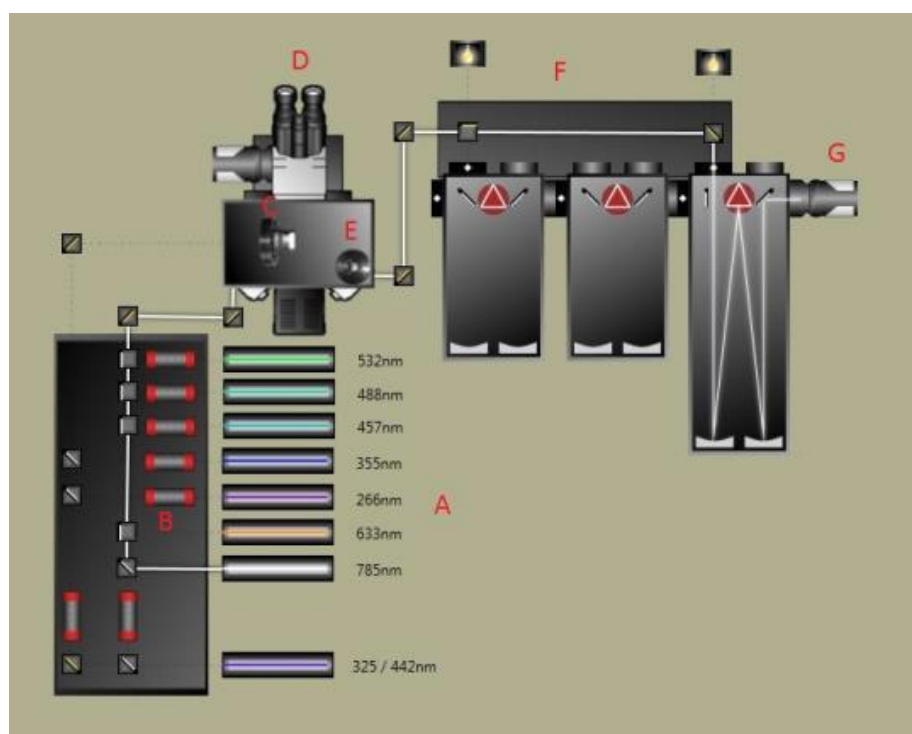

Figure 9. Schematic diagram of the multi-laser Raman spectroscopy setup. A: laser source; B: beam expander; C: neutral density filter; D: optical microscope; E: edge filter; F: TriVista triple grating.

An optical microscope (Olympus) was employed to focus the laser beam onto the sample. The application of microscope enables higher spatial resolution. [40] The optical microscope was mounted at the entrance of the Raman spectrograph, and Raman excitation and collection were both performed using X10 objectives for VIS range lasers and XUV objectives for UV range lasers.

In catalysis research molecular-level understanding of relationships between catalyst structure and activity/selectivity of the catalyst in a specific reaction requires that these properties have to be simultaneously analyzed while the reaction is really happening.[40] Due to the complexity of the mode of operation of catalysts, generally more than one method is required to establish meaningful structure-activity relations, and this system's necessity was stated by various researchers.[41] For this purpose the term o*perando* was created to express a methodology that realizes in situ spectroscopic characterization and activity measurements together in a single experiment. The word "*operando*" stems from the Latin word for "working".

To analyze catalysts at elevated temperatures and in the flow of a gas, the catalyst powder was placed into a Linkam CCR1000 reaction chamber from Linkam Scientific Instruments implemented in the confocal Raman microscope. The cell used for the reactivity study of the surface oxygen species toward CO, propane, and propylene is illustrated in Figure 10.
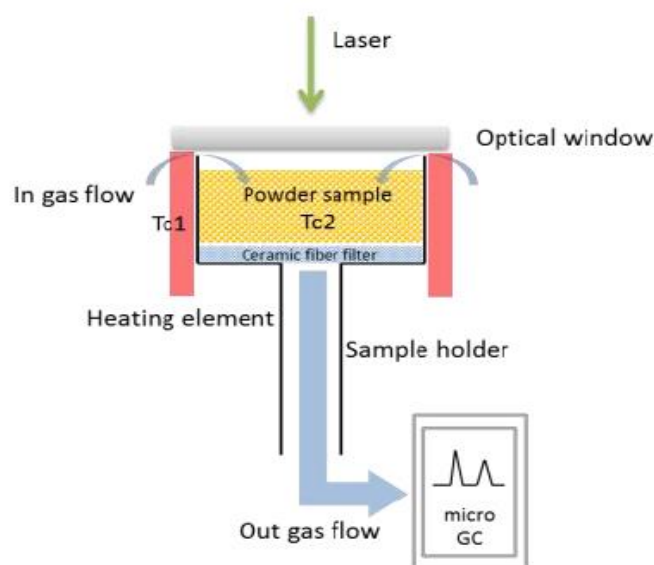

Figure 10. Detailed sketch of Linkam CCR1000 reaction cell

The powdered sample, approximately 20 mg, was densely loaded into the ceramic sample holder. There are two thermocouples in this reaction chamber. One is located at the inner wall of the sample holder for temperature controlling (Tc1). Another is inserted into the sample to measure the actual reaction temperature (Tc2). The gases for experiments are delivered by mass flow controllers, for example, He, O_2, Ar, propane/propylene, and CO with the flow rate of 20ml/min. The gases flow from top to bottom of the cell passing through the powdered sample which is carried on a ceramic fiber filter. The outlet of the gas flow from the cell is connected to a mGC (490 Micro GC, Agilent) to perform online gas product analysis. So, catalytic activities for CO and propane oxidation of different CeO_2 samples can be investigated in a qualitative and quantitative way.

To enable even faster gas phase analysis and isotope exchange experiments, a mass spectrometer (MS, GSD 320 Omnistar from Pfeiffer vacuum) was employed. The effluent gas composition of mixtures and their relative concentrations were analyzed continuously during the whole experiment, and different fragments in the form of mass to charge (*m/z*) ratios were tracked. The expected fragments have been selected based on the gas phase analysis by the mGC.

2.4   Activation process

As the high oxygen storage capacity of CeO_2 originates from oxygen vacancies, which can be easily formed and removed depending on temperature and gas phase composition, these defects, can be considered as the most reactive sites on CeO_2. Theoretically, in the defect chemistry of bulk CeO_2, the loss of oxygen and the reduction of Ce^{4+} to Ce^{3+} are accompanied by creation of the oxygen vacancies. Electrons, which are released from the vacancy sites are back-donated to localized Ce_{4f} states and mobile by a small-polaron hopping process.[42] Reduced non-stoichiometric CeO_2, therefore, is a mixed ionic/electronic conductor. It is possible to form and enhance the concentration of oxygen vacancies by heating CeO_2 at elevated temperatures under vacuum, or reducing it by applying reducing agents at certain temperatures.[11, 43] The non-stoichiometric composition of CeO_{2-x} and the presence of oxygen vacancies are important in oxidation catalysis.[20, 44]

To compare the three cerium oxides with different morphology, a defined pre-treatment procedure (activation process) was performed before starting the adsorption and reactivity experiments. The activation process was carried out with a flow of inert gas (He) at a flow rate of 20ml/min, heating up to 673K with a heating rate of 5K/min, holding for 1 hour, and then cooling down to room temperature (303K).

3 Results & Discussion

3.1 Raman spectra of CeO_2

Theoretically, the fluorite-type cubic crystal structure of CeO_2 exhibits only one Raman active fundamental mode at 464 cm^{-1}, which is the triply degenerate F_{2g} mode that corresponds to a symmetric Ce-O stretching vibration in the O_h point group. It can be regarded as symmetric breathing mode of six oxygen atoms around the central cerium ion.[45] Peaks near 260, 600, and 1170 cm^{-1} are attributed to the second-order transverse acoustic (2TA) mode, a defect-induced (D) mode, and the second-order longitudinal optical (2LO) mode, respectively. Generally, it has been reported that defect-induced peaks are more strongly pronounced under UV excitation due to resonance Raman effects since CeO_2 strongly absorbs in the UV region.[46]

Before *in-situ* experiments were started, the beam sensitivity of the particle sample was analyzed to minimize damage caused by strong laser power and to adjust and optimize the energy density. Raman spectra of the sample were collected varying the filters in the range ND = 1.0 to 3.0 resulting in laser powers from 1.4 mW to 0.014 mW, respectively. The exposure time was kept constant at 60s. For all Raman studies performed in this thesis, the laser power was adjusted to below 0.2mW for VIS range lasers, and 0.8mW for UV range lasers, respectively.

3.1.1   Influences of activation on the Raman spectra of CeO$_2$

The Raman spectra of the three nano-structured CeO$_2$ catalysts were collected before and after activation using laser excitation wavelengths at 325, 532, 488, and 633 nm, respectively. The spectra are shown in Figure 11. As discussed above, the main band at 464 cm^{-1} is assigned to the F$_{2g}$ mode of the fluorite-type structure of CeO$_2$. After activation a partial increase in the intensity of peak at 590 cm^{-1} due to the defect-induced (D) mode was observed especially when the 325 nm laser was used.[22h, 45a, 45b, 46a, 47] The D band at 590 cm^{-1} is due to Frenkel-type oxygen vacancies, which start to form on the surface/subsurface and progress into the bulk of ceria. Their amount is affected by the surface termination of CeO$_2$.[48] Frenkel-type oxygen vacancies are most abundant in nanorods (Figure 11 b).

However, we also observe a significant increase in the defect concentration after activation in He at 673 K in particular for the particle sample.

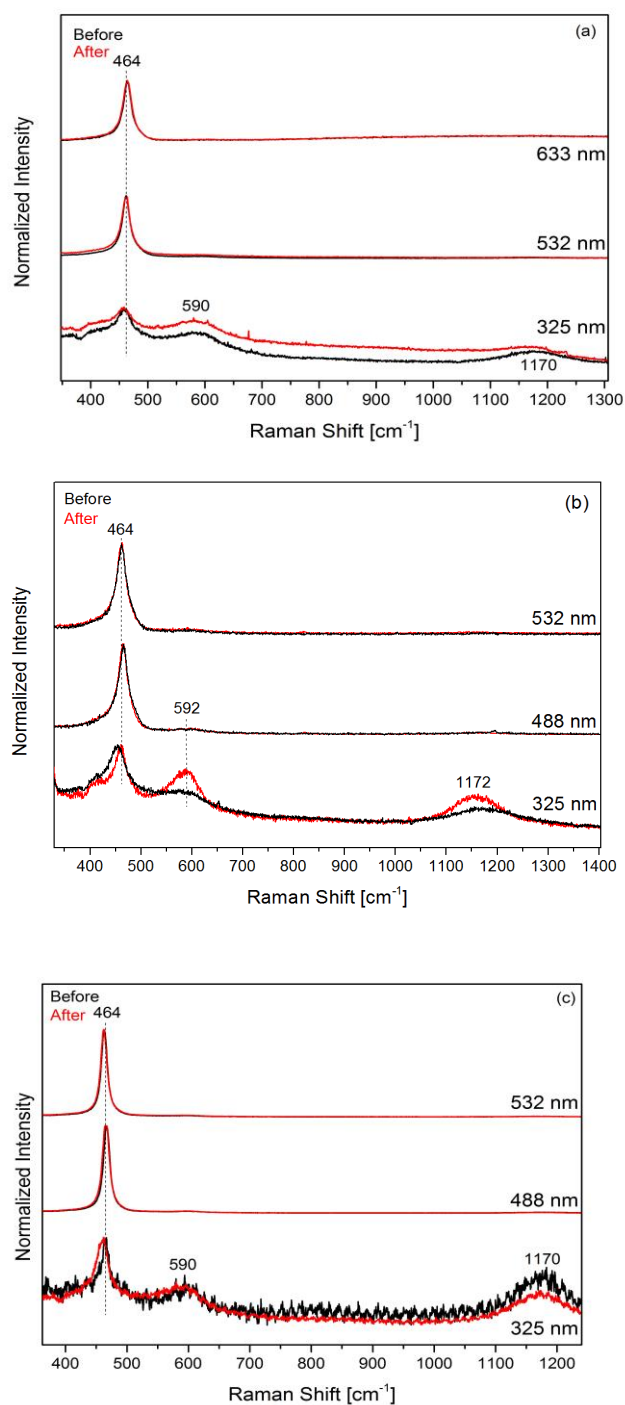**Figure 11. Raman spectra of ceria using visible (λ$_{ex}$=532 nm, 633 nm) and UV (λ$_{ex}$ =325 nm) laser before (black lines) and after (red lines) activation at 673K in He for 1h. (a) Particle, (b) nanorod, and (c) nanocube. The Spectra are normalized by intensity at 464 cm^{-1}, F2g mode.**

3.2 Oxygen (O₂) adsorption on CeO₂

Adsorption of oxygen and transfer of electrical charge results in an increase in the O-O bond length of adsorbed O_2 and finally in dissociation of the molecule, which can be observed by Raman spectroscopy. Metal oxides treated at elevated temperatures in absence of oxygen or at low partial pressure of oxygen provide low-coordinated metal cations as adsorption sites. The strength of oxygen adsorption on metal oxide surfaces varies in a broad range from interaction based on dispersive forces to formation of a chemical bond. Due to an increase in bond length with increasing electron transfer a red shift of the O-O stretching vibration frequency is observed by going from adsorbed molecular oxygen (O_2, ca. 1550 cm^{-1}), to superoxide O_2^{2-} (ca. 1140 cm^{-1}), and peroxide O_2^{-} (ca. 840, 860, and 890 cm^{-1}) depending on the degrees of defect aggregation).[49] Also because of different morphologies, it is possible to expect different oxygen species on CeO_2 samples.

These different oxygen species with variable electrophilic character are kinetically significant intermediates in various oxidation reactions catalyzed by CeO_2. Thus, a detailed study of the surface oxygen species is required.[34, 50] The general reaction sequence during oxygen dissociation follows the equation

$$O_{2\ ads} \rightarrow O_{2\ ads}^{-} \rightarrow O_{2\ ads}^{2-} \rightarrow 2O_{ads}^{-} \rightarrow 2O_{lc}^{2-}$$
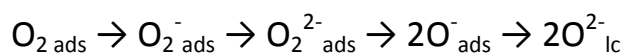
where the $2O_{lc}^{2-}$ is a lattice oxygen ion. The formation of the intermediate species is dependent on the electron donation ability of the surface and the abundance of optimal sites for stabilizing the formed species.

3.2.1 $^{16}O_2$ adsorption on CeO_2

O_2 adsorption on activated CeO_2 was carried out with 20% O_2/He at a flow rate of 20ml/min at room temperature (303 K). Raman spectrosocpy was performed to characterize different oxygen species on different CeO_2 surfaces.
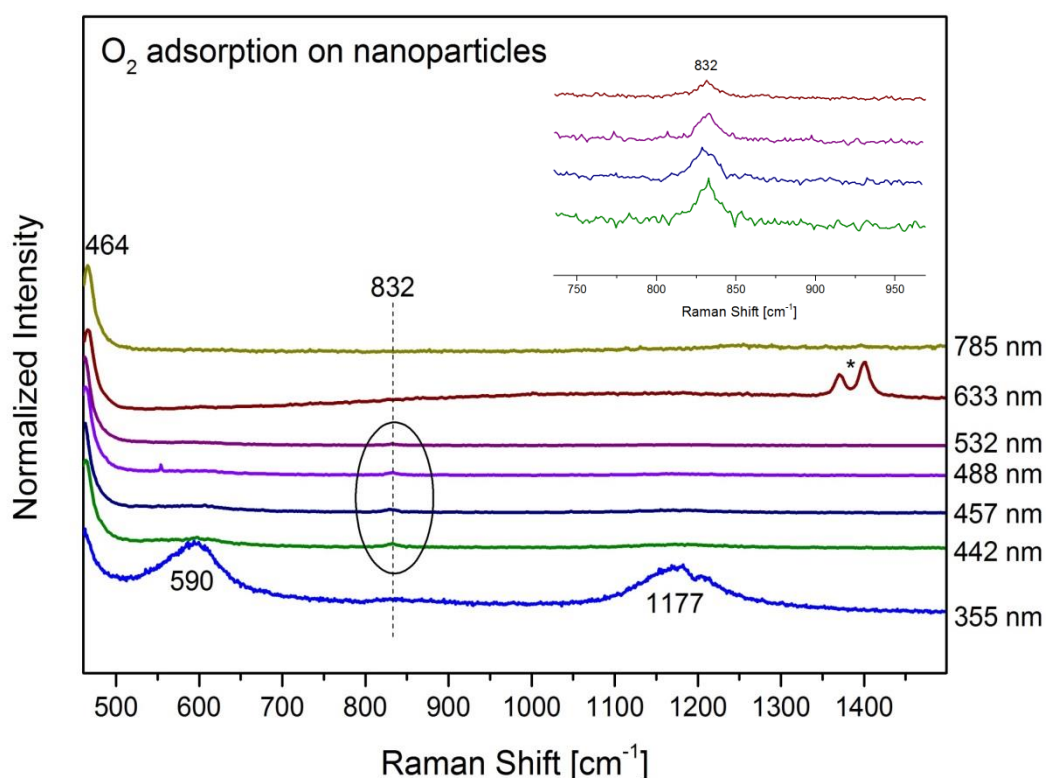
Figure 12. Raman spectra of particles in flowing 20% O_2/He at room temperature (303 K) with different laser excitations. Asterisk (*) indicates carbonate species from synthesis procedures. The spectra are normalized by intensity at 464 cm^{-1}, F_{2g} mode.

Exposure of the activated CeO_2 particle sample to O_2 at room temperature results in the appearance of one band at 832 cm^{-1} (Figure 12). Throughout O_2 adsorption experiment on nanoparticles under all different laser excitations, lasers in the visible range (442, 457, 488, and 532 nm) are suitable to investigate this Raman band, and 488nm excitation is the most suitable one in terms of the absolute intensity of the peak. This Raman band is assigned to the O-O stretching vibration of adsorbed peroxide species, O_2^{2-}, which are adsorbed on

isolated two-electron defect sites.[51] Subsequent experiments with nanocubes and nanorods exhibit also the same adsorbed oxygen species at identical position (832 cm^{-1}) when the 488 nm laser is used for excitation, even though the surface of the nanoparticles with different morphology have different terminating crystal planes (Figure 13). This implies that the local structure of the adsorption site seems to have no significant impact on the O - O band strengths in the adsorbed peroxide ion.
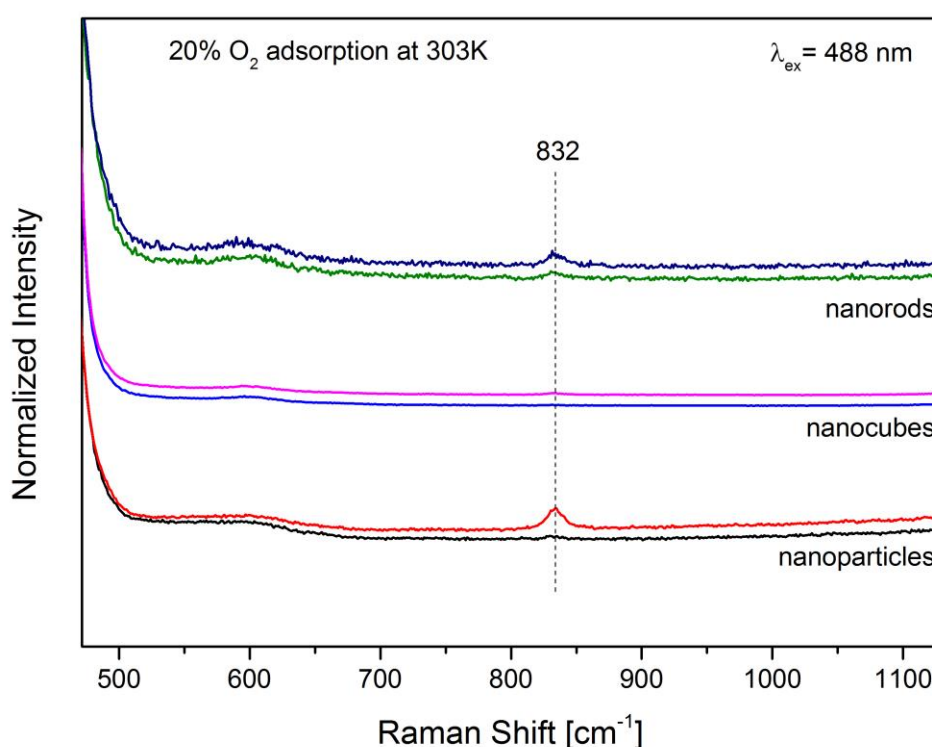
Figure 13. Comparison of Raman spectra before and after O$_2$ adsorption at room temperature (303 K) on the three different nanostructured CeO$_2$ samples. The Raman band at 832 cm^{-1} is assigned to adsorbed peroxide species. The Spectra are normalized by intensity at 464 cm^{-1}, F$_{2g}$ mode.

So, the nature of adsorbed oxygen species is similar on the three different CeO_2 surfaces (Figure 13).

The evolutions of the peroxide bands with time at 303K in 20% O_2/He flow (20ml/min) shown in Figure 14. For all samples, adsorption happens right after exposure of the samples with oxygen, and reached the maximum intensity of the peak at 832 cm^{-1} is reached after a few minutes. The peak intensity of nanocube (b) at 832 cm^{-1} is very low (Figures 13-14) due to the lower specific surface area of the nanocube sample compared to other samples. Differences in the kinetics of peroxide formation have been discussed in the literature based on the stability of oxygen vacancies on different facets.[9, 25b] Unfortunately, the defect-induced peak at 600 cm^{-1} observed after the activation process on all three ceria samples is observable best by using the 325 nm laser for exitation (Figure 11). Under the same measurement conditions the formation of peroxide species cannot be observed in the Raman spectrum (Figure 14). That means the consumption of oxygen vacancy sites during formation of peroxide species cannot be monitored in the same experiment.
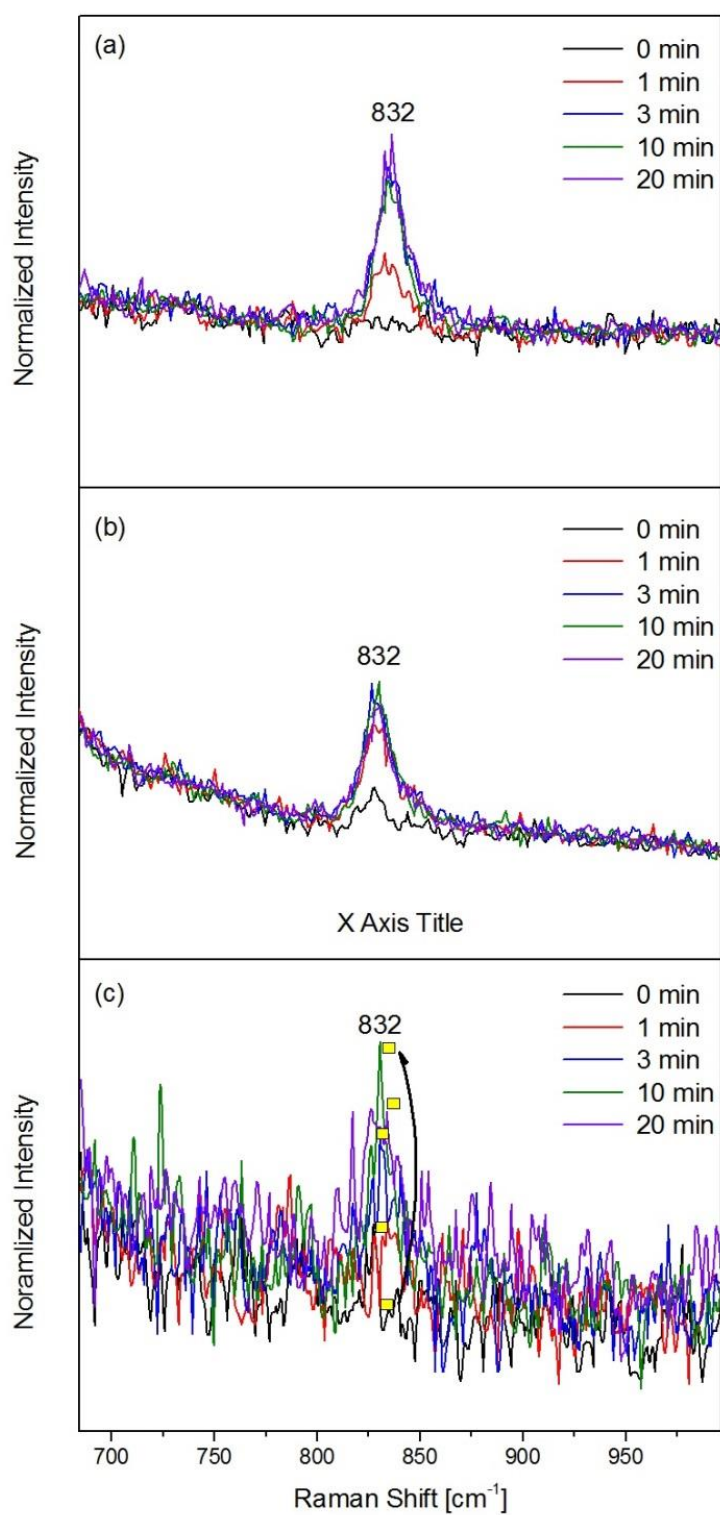
Figure 14. Raman spectra collected during 20% O₂ adsorption at room temperature (303 K) for 20 min on (a) particle, (b) nanocube, and (c) nanorod applying the 488 nm laser for excitation.

3.2.2 $^{18}O_2$ adsorption on CeO₂

To verify that the peak at 832 cm^{-1} observed upon $^{16}O_2$ adsorption at room temperature on CeO₂ is originated indeed from adsorbed oxygen species, an oxygen isotope exchange experiment was carried out. [49a] The Raman spectra of the particle sample after adsorption of $^{18}O_2$ applying lasers at 442, 457, and 488 nm for excitation are shown in Figure 15.
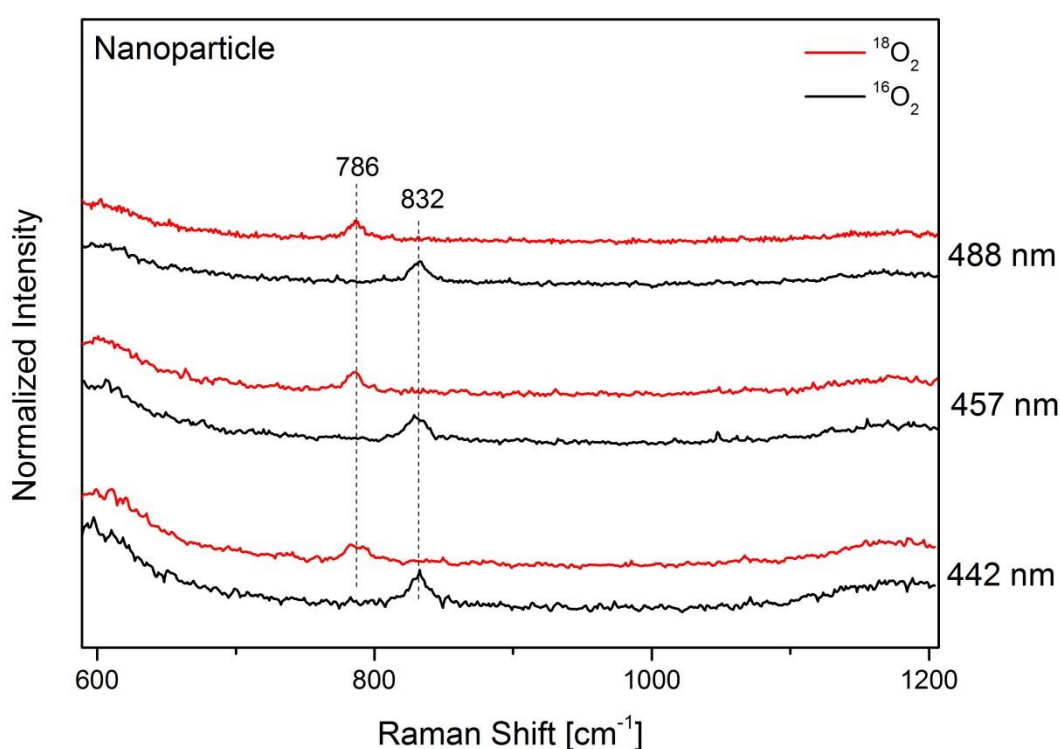
Figure 15. Comparison of Raman spectra of the particle sample in flowing $^{16}O_2$ (black lines) and $^{18}O_2$ (red lines) (20% O₂/He) applying lasers in the visible range for excitation at room temperature (303 K).

At first, adsorption of $^{16}O_2$ was performed. Before switching the gas feed to $^{18}O_2$, He was purged to remove pre-adsorbed $^{16}O_2$ on the surface of CeO₂ nanoparticles. By exposing $^{18}O_2$ (20% $^{18}O_2$/He, 20ml/min) to CeO₂ after the $^{16}O_2$ adsorption experiments at room temperature, the peak corresponding to peroxide species adsorbed on the ceria nanoparticles was shifted to 786 cm^{-1} indicating complete exchange of adsorbed $^{16}O_2^{2-}$ by gas phase $^{18}O_2$ at room temperature. The measured peak shift expressed by the ratio of the peak positions (1.059) is in a good agreement with the theoretical value of 1.061 assuming a diatomic oscillator.

Therefore it is concluded that the peak at 832 cm^{-1} observed upon oxygen adsorption on the CeO$_2$ surface can indeed be attributed to adsorbed peroxide species.[51a, 52]

In summary, it was shown that O$_2$ adsorption on nanostructured CeO$_2$ samples results in the formation of adsorbed peroxide species that are stable at room temperature. The involvement of oxygen vacancies generated during the activation process in helium in the formation of peroxide species is assumed. Direct experimental evidence, however, requires further kinetic studies of the disappearance of the defect-induced band at 600 cm^{-1} upon contact with oxygen using a 325 nm laser as excitation source.

3.3 Oxygen adsorption on CeO$_2$ in presence of a reducing agent in the gas phase

Based upon the fact that CeO$_2$ could easily be reduced and the oxygen vacancies within its structure possess high mobility, the material has been studied in oxidation reactions such as CO oxidation and propane oxidation.[53] These reactions can be considered as probe reaction for the surface redox properties of CeO$_2$. Adsorbed oxygen species, such as the peroxide species described above, will react with CO and propane. Furthermore, the oxygen defects present on the surface of ceria or, in other words, co-ordinatively unsaturated ceria species, are important for adsorption of CO and propane.

The abundance of adsorbed peroxide species on the surface of the nanostructured ceria catalysts was monitored in temperature-programmed experiments of CO and propane oxidation, respectively. For the oxidation reactions, 5% CO in a mixture of 20% O$_2$ in He flow and 2% CO in a mixture of 15% O$_2$ in He flow (total flow rate 20ml/min) were introduced into the Raman cell and the temperature was increased up to 553 K using a heating rate of 5K/min. At the same time the Raman spectra were recorded and the composition of the effluent gas was analyzed by gas chromatography.

3.3.1 CO oxidation

In CO oxidation over CeO_2 the surface itself has been considered to be actively involved in the reaction according to a Mars-van Krevelen-type mechanism under stationary condition in the presence of gas phase O_2.[11, 28] CO is adsorbed and reacts with a surface oxygen species under formation of CO_2. The reaction product desorbs, a vacancy is left behind in the surface with the metal ion in lower oxidation state. In principle the vacancy will be filled again by oxygen from gas phase. It has been frequently observed that CO oxidation over nanocrystalline CeO_2 is structure sensitive due to the exposure of different surface terminations on rods ((110) + (100)), cubes (111), and crystals with octahedral shape (111).[28]

In the present experiments, the oxidation of CO (CO + ½ O_2-> CO_2) was analyzed by using a gas chromatograph (GC) equipped with a thermal conductivity detector. A gas mixture of CO (5%) and O_2 (2%) balanced with helium was used as reaction feed. The conversion of CO was calculated based on the carbon atom balance using the following formula, where N represents the relative percentage of reactant or product in the product stream. X_{CO} represents the conversion of CO. The selectivity to CO_2 is always 100%, because no other product except CO_2 can be formed in CO oxidation.

$$X_{CO} = \left\{ 1 - \left(\frac{N_{CO}}{N_{CO} + N_{CO_2}} \right) \right\} * 100$$

3.3.1.1 Raman spectroscopy during CO oxidation over particles

The CeO$_2$ particle sample (20mg) was exposed to the CO oxidation feed in the Linkam CCR1000 chamber. After 30 min steady-state operation at 553 K the gas was switched to He (20ml/min). The evolution of the Raman peak intensity of peroxide species at 832 cm^{-1} was monitored by Raman spectroscopy (green data points). The conversion of CO was followed by online mGC (black data points). Raman results and reactivity data are presented in Figure 16.

The intensity of the Raman band due to adsorbed peroxide species at 832 cm^{-1} starts to decrease at a temperature at which the CO conversion becomes measurable. This means that adsorbed peroxide species might be involved into CO oxidation. However, it is no proof, because the measured intensity may simply reflect the steady-state concentration of peroxide species present on the surface. The carbon dioxide may be formed by reaction with surface lattice oxygen species generating defects at which the peroxide species are formed by adsorption and partial reduction of gas-phase oxygen.
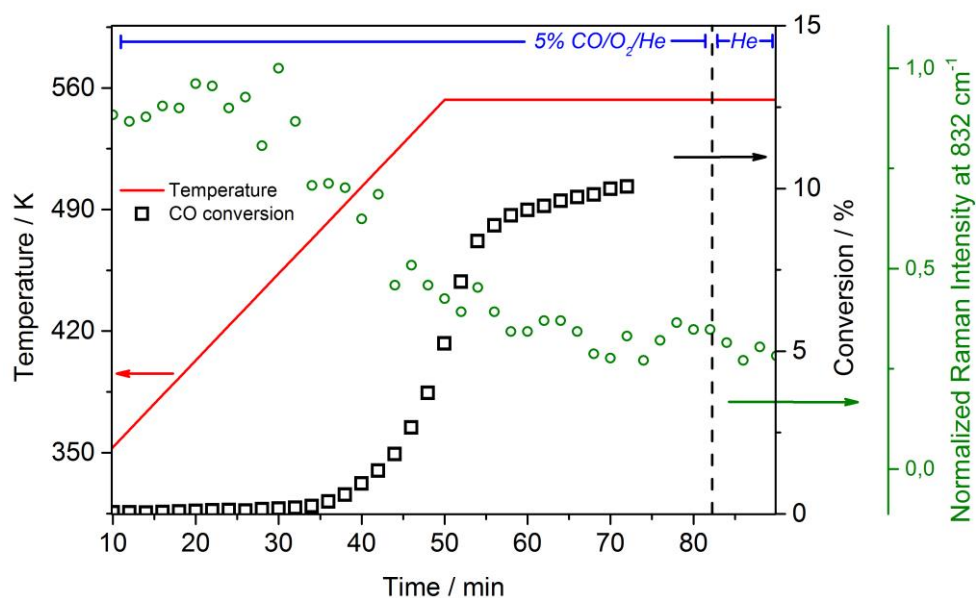
Figure 16. Raman peak intensity at 832 cm^{-1} and conversion of CO as a function of temperature in CO oxidation over the particle sample.

3.3.1.2 Raman spectroscopy during CO oxidation over rods

On CeO$_2$ rods (20mg) the same experimental procedure was applied. As shown in Figure 17, the Raman peak intensity of the band at 832 cm^{-1} increases with increasing temperature in a range where CO conversion is still zero indicating that oxygen vacancies are formed just due to a thermal effect. Gas-phase oxygen is then adsorbed on these defects under formation of peroxide species. Again, the intensity of the Raman band due to adsorbed peroxide species at 832 cm^{-1} starts to decrease at a temperature at which the CO conversion becomes measurable. The rods are slightly more active (X=13%) compared to the particles (X=10%) at the final reaction temperature of 553 K.

Since the intensity of the peak due to adsorbed peroxide species was much smaller on the cube sample due to its low specific surface area, the experiment was not performed for the cubes.

Figure 17. Raman peak intensity at 832 cm^{-1}and conversion of CO in increasing temperature (left), comparison between conversion of CO and selectivity for CO$_2$ from CO oxidation (right) over nanorods.

3.3.2 Propane oxidation

Propene is produced on a large scale by steam cracking of naphtha, fluid catalytic cracking (FCC), methanol to olefins (MTO), and dehydrogenation of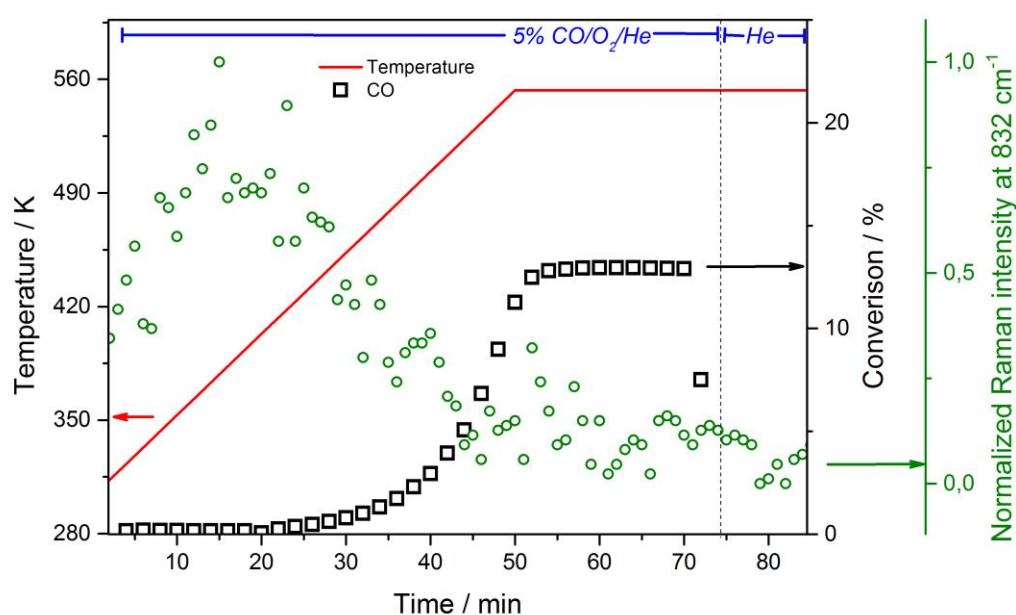 propane (PDH).[54] The direct conversion of propane into propene by partial oxidation with molecular oxygen is economically and ecologically interesting.[55] Propane is abundant and cheap, also its oxidation process can result not only in high value propene but acrolein, acrylic acid, and acrylonitrile. All these valuable products are applied as monomers for polymerization. However, the reaction is not applied in industry due to so far insufficient low selectivity. The activation of oxygen is the key reaction step in alkane oxidation that has a major impact on the undesired total oxidation of propane to CO_2.[56] The research aim in the field of oxidation catalysis is to control selectivity by understanding the reaction mechanism and structural requirements of the catalyst for selective activation of the reactants propane and oxygen.

In an attempt to investigate the oxygen activation over ceria in presence of propane, CeO_2 particles and nanocubes will be examined. As evidenced by gas chromatography, propene and CO_2 are the only products formed in propane oxidation over ceria under the applied reaction conditions. The conversion of propane and selectivity towards propene and CO_2 was calculated by a carbon atom balance method using the following formulas, where N represents the relative percentage of gas phase components in the product streams. $X_{C_3H_8}$, $S_{C_3H_6}$ and S_{CO_2} represent the conversion of propane and the selectivity to propylene and CO_2 respectively.

$$X_{C_3H_8} = \left\{ 1 - \left(\frac{N_{C_3H_8}}{N_{C_3H_8} + N_{C_3H_6} + N_{CO_2}} \right) \right\} * 100$$

$$S_{C_3H_6} = \left\{ \frac{N_{C_3H_6}}{(N_{C_3H_6} + N_{CO_2})} \right\} * 100$$

$$S_{CO_2} = \left\{ \frac{N_{CO_2}}{(N_{C_3H_6} + N_{CO_2})} \right\} * 100$$

3.3.2.1 Raman spectroscopy during propane oxidation over particles

On the CeO_2 particle sample (20mg) a gas feed of 2% C_3H_8/15% O_2/83% He was introduced and the temperature was increased up to 553 K at a rate of 5K/min. At the reaction temperature of 553 K the reaction was performed for 30 minutes. Then, the gas was switched to He (20ml/min). The evolution of the Raman peak intensity of peroxide species at 832 cm^{-1} was monitored by Raman spectroscopy, while propane, CO_2, and propene were analyzed by online mGC.
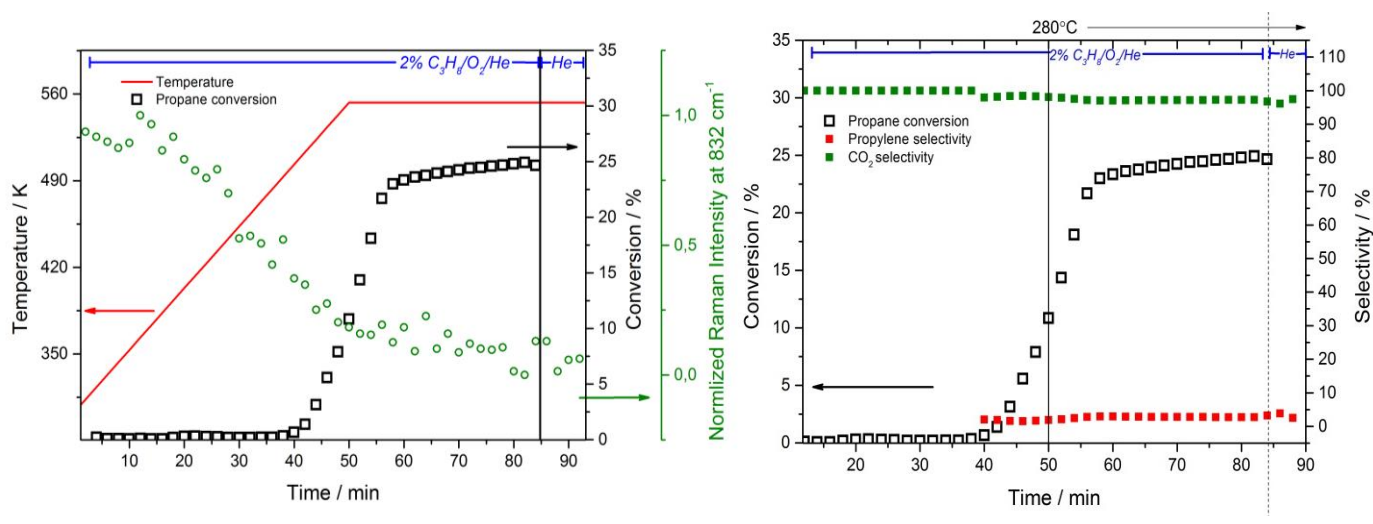
Figure 18. Raman peak intensity at 832 cm^{-1} and conversion of C_3H_8 as a function of the temperature (left), comparison between conversion of propane and selectivity to the products (right) over the particle sample.

Figure 18 illustrates the results. On the left side the intensity of the Raman band due to adsorbed peroxide species is compared with the conversion of propane. The selectivity to propene and CO_2 is plotted as a function of reaction temperature and time on the right side. At about 513 K the conversion of propane started to increase and at 553 K a stable conversion of 23 - 24% propane was observed for another 30 minutes. The main product in

propane oxidation on the particle sample was CO_2, and at slightly higher temperatures (>473 K) propylene was produced but with very low selectivity (maximum ca. 5%).

There is no correlation between the decrease in intensity of the Raman band due to adsorbed peroxide species at 832 cm^{-1} and the onset of propane conversion. The intensity starts to decrease at a similar temperature as in the CO oxidation experiment (compare Figure 17 and 18) suggesting that the intensity decrease is due to thermal desorption and/or further reduction/dissociation of adsorbed peroxide. It should be noted at this point that the peroxide species adsorbed on CeO_2 are detectable in inert gas (in absence of oxygen or oxygen/CO or oxygen/propane mixtures) only up to 345 K. The observation indicates that peroxide species on the surface detected at elevated temperatures in presence of oxygen and a reducing agent reflect a steady-state concentration of these species in the process of oxygen reduction.

3.3.2.2 Raman spectroscopy during propane oxidation over cubes

The propane oxidation experiment over the CeO_2 cube sample (20mg) is presented in Figure 19.
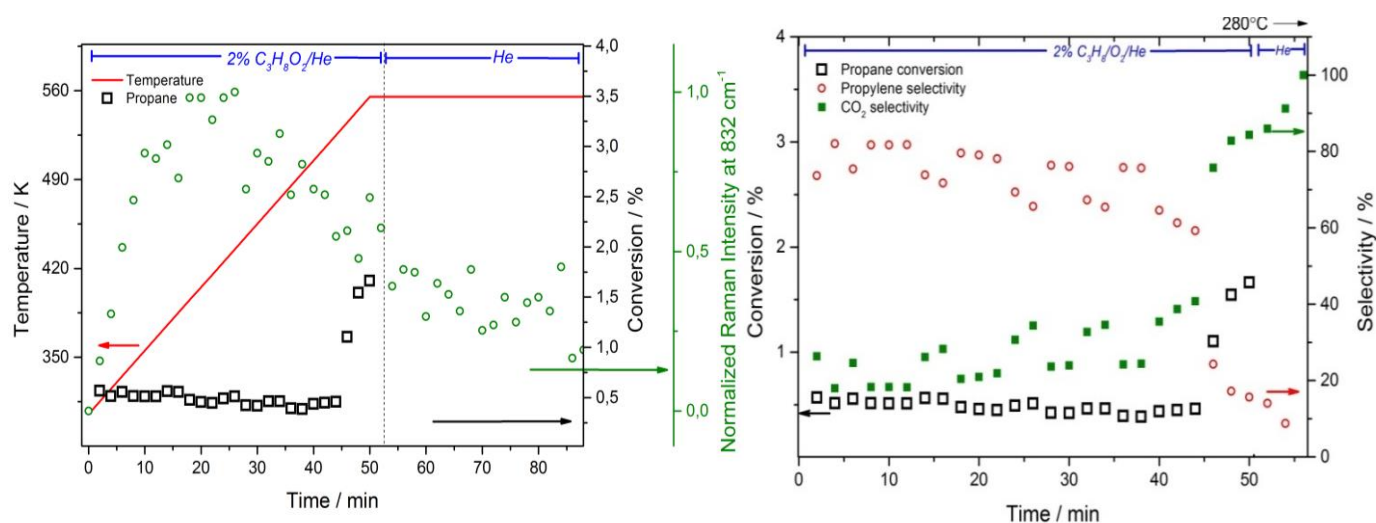
Figure 19. Raman peak intensity at 832 cm^{-1}and conversion of 2% of C_3H_8 in increasing temperature (left), comparison between conversion of propane and selectivity of products from propane oxidation (right) over nanocubes.

Due to the 4 times lower surface area compared to the CeO_2 particle sample, the cubes show a very low propane conversion (1.5%). Nanocubes are 3 times less active than particles. Therefore, the selectivity data are less accurate. The selectivity to propene is higher on cubes compared to particles due to the much lower conversion of propane on the cubes.

The peak intensity at 832 cm^{-1} due to adsorbed peroxide species increases until the reaction temperature of 553 K was reached indicating that propane oxidation generates oxygen vacancies that facilitate peroxide species formation. This observation is in good agreement with the morphology of the CeO_2 nanoparticles. CeO_2 cubes mainly expose (100) surface facets, which have been shown to require less energy to form oxygen vacancies compared

with (111), and (100) surfaces, which are abundant on particles. But there seems to be no correlation between the concentration of adsorbed peroxide species or generated oxygen vacancies with the catalytic activity in propane oxidation.

In summary, the experiments revealed different catalytic activity of CeO_2 nanoparticles in CO and propane oxidation reactions even though all morphologically different ceria samples stabilize O_2 as peroxide species (832 cm^{-1}). A direct correlation between the abundance of these species and the catalytic activity or the selectivity in propane oxidation was not observed

3.4   Reactivity of adsorbed peroxide species in pulse experiments

On the surface of metal oxides including CeO_2, the nature of the reacting oxygen species in oxidation reaction is less obvious. The situation is complex, because both adsorbed surface oxygen species and lattice oxygen can participate in the reaction depending on the oxide used and the reaction conditions with respect to temperature and redox potential of the gas feed.

Throughout CO and propane oxidation experiments, oxidation reactions on the CeO_2 surface are occurring. The nature of the responsible oxygen species, namely whether the oxidation reaction occurs under involvement of lattice oxygen or adsorbed oxygen species, is still unclear. In previous studies in the literature the lattice oxygen rather than the adsorbed or gaseous oxygen was attributed to oxidation reactions under the typical high reaction temperatures.[28] So the reactivity and mobility of lattice oxygen as well as adsorbed peroxide species with pulses of propene in presence of either $^{16}O_2$ or $^{18}O_2$ over the CeO_2 particle sample was studied by Raman spectroscopy and mass spectrometry.

Before discussing the experiment, a matrix of expected fragments from propane oxidation and their mass to charge ratios (*m/z*) are presented in Table 3.

Table 3. Matrix of expected mass/charge ratios of possible products from propene oxidation reaction. Number without under line means products with ^{16}O in the product, and <u>underlined numbers</u> correspond to mass/charge ratios with ^{18}O in the product.

m/z	Ar	He	O₂	CO	CO₂	Propene	2-Propen-1-ol	acetone	Propanal	2-propenal	Acetaldehyde	Propanoic acid	2-Propenoic acid	Acetic acid	Ethylene
4		X													
18/16			X	X	X										
27										X					
30/28				X	X							X			X
29									X		X	X			
31							X								
34,36/32			X												
39						X									
40	X														
42						X									
45/43								X						X	
46,48/44					X						X				
47/45												X		X	
55										X			X		
56										X					
59/57							X								
58								X	X						
62/60														X	
72													X		
76/74												X			

3.4.1 Propene pulse together with $^{16}O_2$

The pulse experiments were started with oxygen adsorption applying a feed of 20% O_2/He (total flow rate 20ml/min) and heating up to 353 K. When the Raman signal of adsorbed oxygen species at 832cm^{-1} was stable, a pulse of 5% propene in a mixture of 5% Ar and 90% He for dilution was introduced into the 20% O_2/He feed and the response of the gas phase composition was followed by mass spectrometry while at the same time the Raman spectra were recorded. The pulse experiment was repeated after 30 minutes. The mass spectra collected show reproducible result for three consecutive pulse experiments. The third pulse experiment is presented in Figure 20.
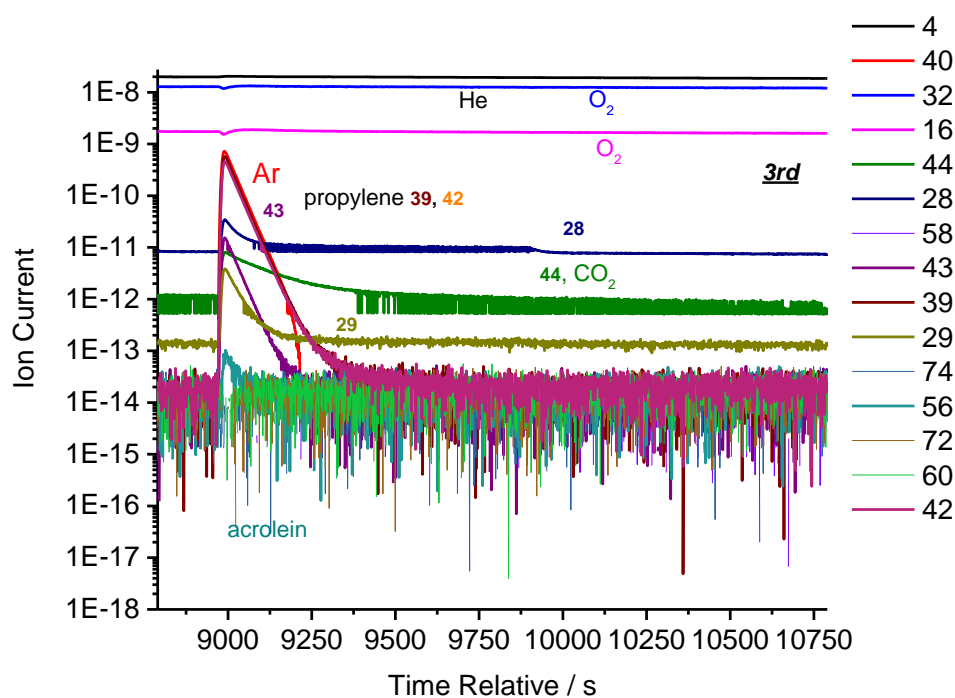

Figure 20. Raw mass spectrometry data of the 3rd propene pulse experiment on CeO₂ particle at 353 K.

To compare the evolution trend of different species within a certain range of time, the spectra have been smoothed and normalized from 0 to 1 (Figure 21). The major signals detected comprise O_2 (32), He (4), Ar (40), propene (39,42), certain oxygenates (43,42), either nitrogen or CO (28), and CO_2 (44). Argon, which does not participate in the reaction, was used as an internal standard. A decrease in the signal for oxygen and possible intermediates was caused by partial pressure drop when the pulse was introduced.
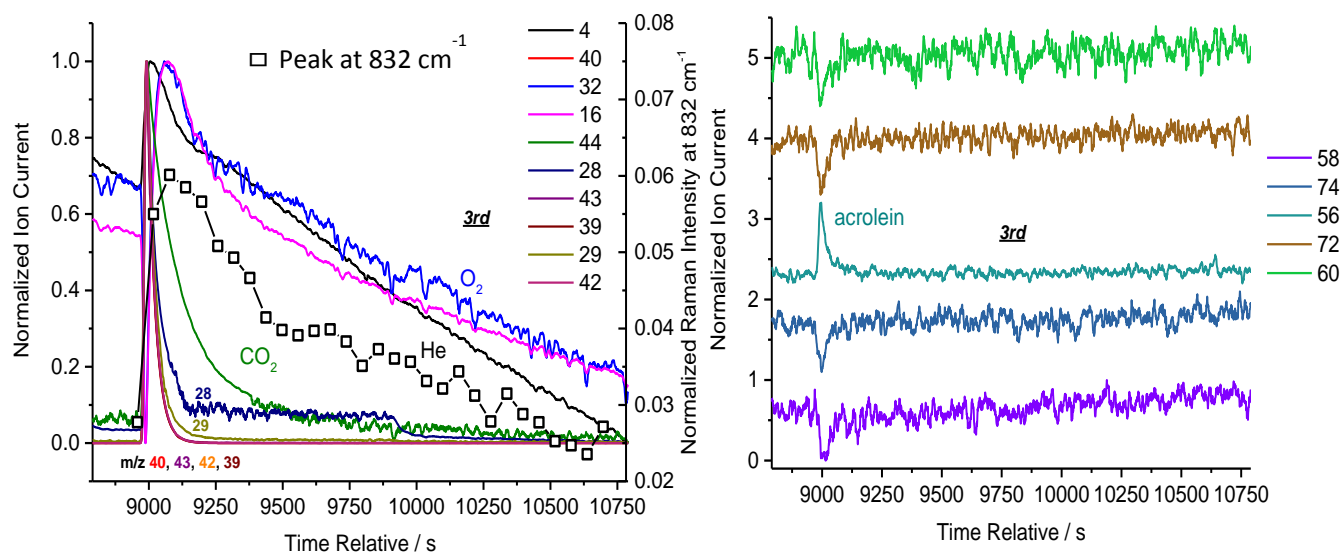
Figure 21. Mass spectra of particle monitored during the $^{16}O_2$ oxidation reaction with 1% propylene pulse at 353 K together with the Raman peak intensity at 832 cm^{-1}(rectangle shaped symbols) (left), mass spectra of signal 56, acrolein, compared with other signals of intermediate species, (right).

In reference experiments it has been shown that the signal 44 does not come from impurities in O_2/He or propene. The profile of the signal 44 differs clearly from the profiles of the other species. The occurrence of the CO_2 signal could be attributed to total oxidation of propene. The signal 56 has a similar trend like signal 44. It is attributed to acrolein, and the signal is shown in the right panel of Figure 21. The drop in other signals present in the background of the mass spectrometer (58 - acetone/propanal, 60 - acetic acid, 74 - propanoic acid, and 72 - 2-propenoic acid) is due to a temporary drop in the partial pressure by introducing the pulse. It is assumed that acrolein is a product, because a positive peak of

m/z=56 was observed upon introduction of the pulse. The Raman peak intensity at 832 cm^{-1} decreases with time. The experiment indicates that the steady-state concentration of adsorbed peroxide species changes with time after introduction of the pulse due to reaction with an organic species or with ceria.

3.4.2 Propene pulse together with $^{18}O_2$

More signals were added to identify the products with $^{18}O_2$. The general trend of the reaction with $^{18}O_2$ is similar to the reaction with $^{16}O_2$. As shown in Figure 22, acrolein (56), (58), CO$_2$ (44), (46), (48), and 2-propen-1-ol (57), propanoic acid (45), (47) were observed based on the mass matrix.
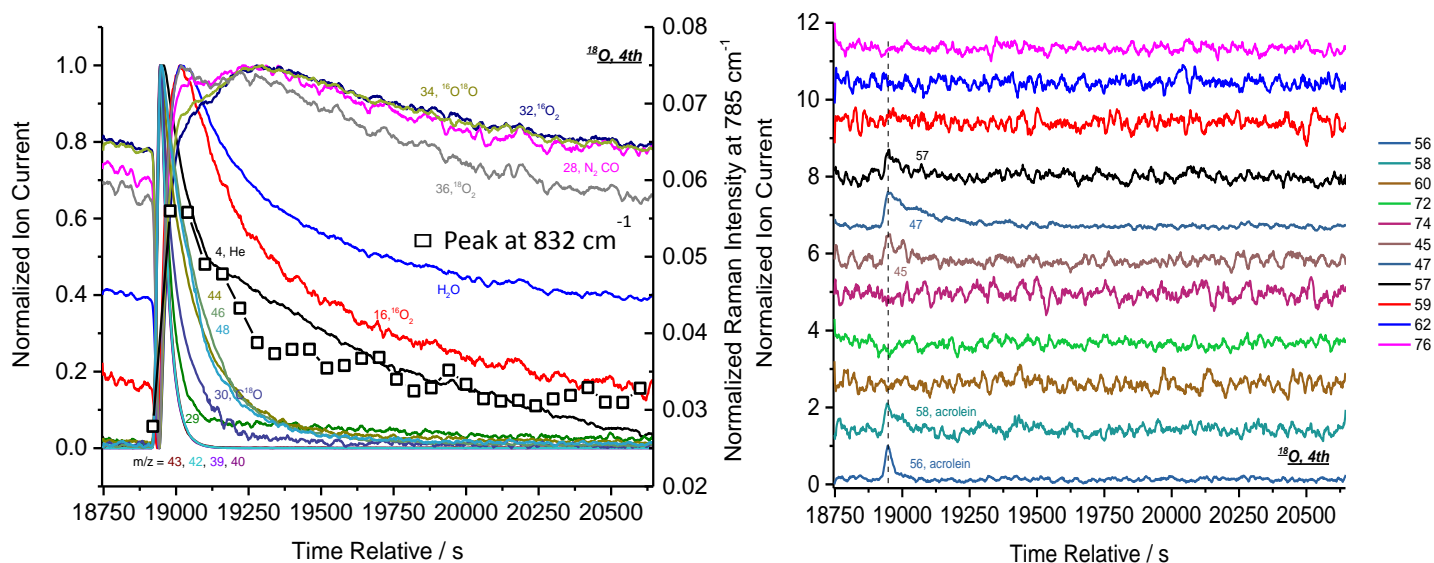
Figure 22. Mass spectra of particle monitored during the $^{18}O_2$ oxidation reaction with 1% propene pulse at 353 K with Raman peak intensity at 832 cm^{-1}(rectangle shaped) (left), Mass spectra of signal 56, acrolein, compared to other signals, (right).

Acrolein, signal 56, was confirmed as product of propene oxidation by the experiment with $^{18}O_2$ (signals 56 and 58(isotope)). Again CO$_2$ is the main product of propene oxidation. It shows three different signals with m/z of 44, 46, and 48 corresponding to C$^{16}O_2$, C$^{18}O^{16}$O, and C$^{18}O_2$, respectively. And the three signals have similar trends but differ from the trend

of He and O_2, so it seems that the three isotopically labeled carbon dioxide molecules are formed by a similar mechanism.

As shown in Figure 23, the signals of the carbon dioxide isotope mixtures exhibit an interesting tendency in terms of their abundance. The contribution of CO_2 with m/z=44 that contains only ^{16}O decreases, whereas the signals due to carbon dioxide that contains also ^{18}O (46, 48, and 30) increase in the consecutive pulse experiments. The formation of CO_2 with m/z=44 in the $^{18}O_2$ experiment is only possibly when the total oxidation of propene occurs under involvement of lattice oxygen. This indicates that the oxygen source for total combustion of propene over ceria can be either adsorbed oxygen ($^{18}O_2$) or lattice oxygen ($^{16}O_2$) in our study. In conclusion, the pulse experiment suggest that lattice oxygen as well as adsorbed oxygen species are unselective oxygen sources in the total combustion of propene over CeO_2, which is in disagreement with results frequently reported in the literature that lattice oxygen is responsible for selective oxidation, while adsorbed oxygen species are responsible for total combustion.
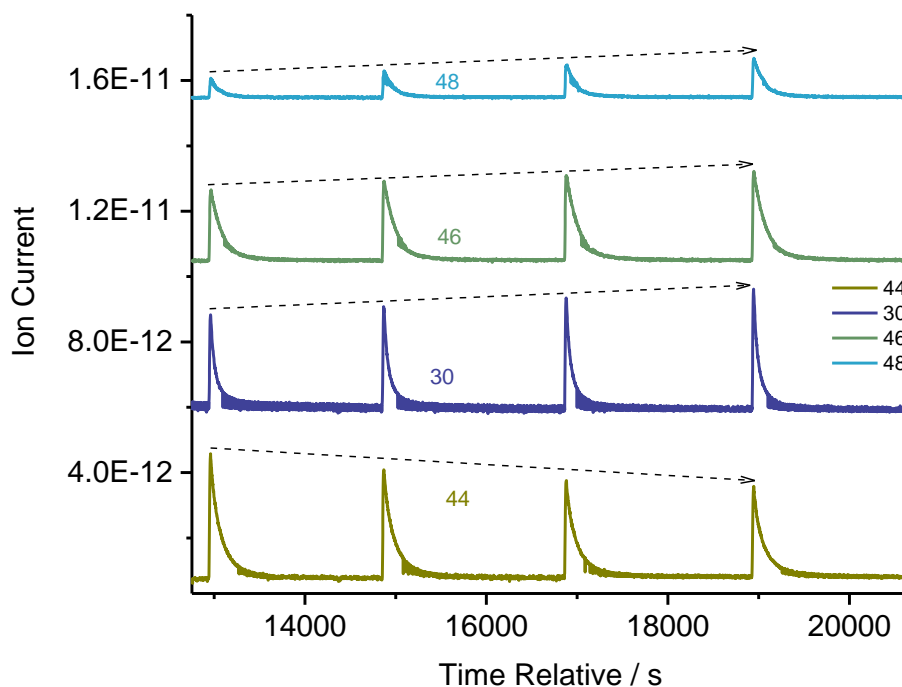

Figure 23. Comparison of amount changes in different COs during 4 pulses of propylene with $^{18}O_2$.

4   Conclusions

Nanostructured CeO_2 with different morphology was studied by *in situ* and *operando* Raman spectroscopy in CO and propane oxidation and by pulse experiments with oxygen/propene mixtures. The CeO_2 samples differ in exposed facets and specific surface area. It is well known that defects such as oxygen vacancies in CeO_2 can play an important role in various catalysis applications. It has been postulated to use modifications in the particle shape to tailor reactivity and selectivity.[1]

The present Raman study revealed that despite differences in the particle morphology of nanostructured CeO_2, oxygen adsorption results in the formation of identical adsorbed peroxide species on the surface characterized by a frequency of the O-O stretching vibration at 832 cm^{-1}.

After activation in He at elevated temperature, oxygen adsorption happened quickly at room temperature on the CeO_2 samples. Theoretically the stability of oxygen vacancies on different facets of CeO_2 follows the order (111) > (100) > (110). Catalytic activity based on oxygen defects is predicted to follow the reverse order.[24, 57]

However, in the *operando* Raman spectroscopic experiments no correlation between the abundance of surface peroxide species and catalytic activity was observed. Furthermore, propene pulse experiments revealed that in the combustion of propene both adsorbed oxygen species as well as lattice oxygen species of CeO_2 are involved. The results contribute to an improved understanding of parameters that control selectivity in oxidation reactions.

Reference list

1.   Lawrence, N. J.; Brewer, J. R.; Wang, L.; Wu, T. S.; Wells-Kingsbury, J.; Ihrig, M. M.; Wang, G. H.; Soo, Y. L.; Mei, W. N.; Cheung, C. L., Defect Engineering in Cubic Cerium Oxide Nanostructures for Catalytic Oxidation. *Nano Lett* **2011,** *11* (7), 2666-2671.

2.   Voncken, J. H. L., Physical and Chemical Properties of the Rare Earths. In *The Rare Earth Elements: An Introduction*, Springer International Publishing: Cham, 2016; pp 53-72.

3.   Trovarelli, A., Catalytic properties of ceria and CeO2-containing materials. *Catal Rev* **1996,** *38* (4), 439-520.

4.   Malavasi, L.; Fisher, C. A. J.; Islam, M. S., Oxide-ion and proton conducting electrolyte materials for clean energy applications: structural and mechanistic features. *Chem Soc Rev* **2010,** *39* (11), 4370-4387.

5.   Fu, M. S.; Wei, L. H.; Li, Y. H.; Zhou, X. Z.; Hao, S. Y.; Li, Y. X., Surface charge tuning of ceria particles by titanium doping: Towards significantly improved polishing performance. *Solid State Sci* **2009,** *11* (12), 2133-2137.

6.   (a) Mandoli, C.; Pagliari, F.; Pagliari, S.; Forte, G.; Di Nardo, P.; Licoccia, S.; Traversa, E., Stem Cell Aligned Growth Induced by CeO2 Nanoparticles in PLGA Scaffolds with Improved Bioactivity for Regenerative Medicine. *Adv Funct Mater* **2010,** *20* (10), 1617-1624; (b) Das, S.; Dowding, J. M.; Klump, K. E.; McGinnis, J. F.; Self, W.; Seal, S., Cerium oxide nanoparticles: applications and prospects in nanomedicine. *Nanomedicine-Uk* **2013,** *8* (9), 1483-1508.

7.   Smets, B. M. J., Phosphors Based on Rare-Earths, a New Era in Fluorescent Lighting. *Mater Chem Phys* **1987,** *16* (3-4), 283-299.

8.   (a) Calaza, F. C.; Xu, Y.; Mullins, D. R.; Overbury, S. H., Oxygen Vacancy-Assisted Coupling and Enolization of Acetaldehyde on CeO2(111). *J Am Chem Soc* **2012,** *134* (43), 18034-18045; (b) Campbell, C. T.; Peden, C. H. F., Chemistry - Oxygen vacancies and catalysis on ceria surfaces. *Science* **2005,** *309* (5735), 713-714.

9.   Conesa, J. C., Computer Modeling of Surfaces and Defects on Cerium Dioxide. *Surf Sci* **1995,** *339* (3), 337-352.

10.   Sayle, T.; Parker, S.; Catlow, C., The role of oxygen vacancies on ceria surfaces in the oxidation of carbon monoxide. *Surf Sci* **1994,** *316* (3), 329-336.

11.   Trovarelli, A., *Catalysis by ceria and related materials*. Imperial College Press: London, 2002.

12.   Skorodumova, N. V.; Simak, S. I.; Lundqvist, B. I.; Abrikosov, I. A.; Johansson, B., Quantum origin of the oxygen storage capability of ceria. *Phys Rev Lett* **2002,** *89* (16).

13.   Clark, J. H., Catalysis for green chemistry. *Pure Appl Chem* **2001,** *73* (1), 103-111.

14.   Council, N. R., *Catalysis Looks to the Future*. The National Academies Press: Washington, DC, 1992; p 96.

15.   Jess, A.; Kragl, U.; Wasserscheid, P., *Chemical technology : an integral textbook*. Wiley-VCH: Weinheim, 2009; p xxxvii, 850 p.

16.   Davis, M. E.; Davis, R. J., *Fundamentals of chemical reaction engineering*. Dover ed.; Dover Publications: Mineola, N.Y., 2012; p xvi, 368 p.

17.   (a) Van Santen, R. A.; Neurock, M., *Molecular heterogeneous catalysis: a conceptual and computational approach*. John Wiley & Sons: 2009; (b) Bligaard, T., Chemical Bonding at Surfaces and Interfaces ed A Nilsson, LGM Pettersson and JK Nørskov. Amsterdam: Elsevier: 2008.

18.   Chapter 1 Introduction. In *Studies in Surface Science and Catalysis*, Kung, H. H., Ed. Elsevier: 1989; Vol. 45, pp 1-5.

19.   Fornasiero, P., *Use of CeO2-based oxides in the three-way catalysts*. 1999; Vol. 50, p 285–298.

20.   Sun, C. W.; Li, H.; Chen, L. Q., Nanostructured ceria-based materials: synthesis, properties, and applications. *Energ Environ Sci* **2012,** *5* (9), 8475-8505.

21.   Vollath, D., *Nanomaterials*. Wiley-Vch: 2013.

22.   (a) Tsunekawa, S.; Sahara, R.; Kawazoe, Y.; Ishikawa, K., Lattice relaxation of monosize CeO2-x nanocrystalline particles. *Appl Surf Sci* **1999,** *152* (1-2), 53-56; (b) Deshpande, S.; Patil, S.; Kuchibhatla, S. V. N. T.; Seal, S., Size dependency variation in lattice parameter and valency states in nanocrystalline cerium oxide. *Appl Phys Lett* **2005,** *87* (13); (c) Tuller, H. L., Ionic conduction in nanocrystalline materials. *Solid State Ionics* **2000,** *131* (1-2), 143-157; (d) Somorjai, G. A.; Tao, F.; Park, J. Y., The Nanoscience Revolution: Merging of Colloid Science, Catalysis and Nanoelectronics. *Top Catal* **2008,** *47* (1), 1-14; (e) Somorjai, G. A.; Kliewer, C. J., Reaction selectivity in heterogeneous catalysis. *React Kinet Catal L* **2009,** *96* (2), 191-208; (f) Geoffrey A Ozin, A. A., Ludovico Cademartiri, *Nanochemistry: A Chemical Approach to Nanomaterials: Edition 2*. Royal Society of Chemistry: Cambridge, U.K., 2008; (g) Chiang, Y. M.; Lavik, E. B.; Kosacki, I.; Tuller, H. L.; Ying, J. Y., Nonstoichiometry and electrical conductivity of nanocrystalline CeO(2-x). *J Electroceram* **1997,** *1* (1), 7-14; (h) Spanier, J. E.; Robinson, R. D.; Zheng, F.; Chan, S. W.; Herman, I. P., Size-dependent properties of CeO2-y nanoparticles as studied by Raman scattering. *Phys Rev B* **2001,** *64* (24).

23.   Branda, M. M.; Ferullo, R. M.; Causa, M.; Illas, F., Relative Stabilities of Low Index and Stepped CeO2 Surfaces from Hybrid and GGA plus U Implementations of Density Functional Theory. *J Phys Chem C* **2011,** *115* (9), 3716-3721.

24.   Wang, Z. L.; Feng, X. D., Polyhedral shapes of CeO2 nanoparticles. *J Phys Chem B* **2003,** *107* (49), 13563-13566.

25.   (a) Zhou, K. B.; Wang, X.; Sun, X. M.; Peng, Q.; Li, Y. D., Enhanced catalytic activity of ceria nanorods from well-defined reactive crystal planes. *J Catal* **2005,** *229* (1), 206-212; (b) W Tasker, P., *The Stability of Ionic Crystals*. 1979; Vol. 12, p 4977-4984.

26.   Sayle, T. X. T.; Parker, S. C.; Catlow, C. R. A., Surface Oxygen Vacancy Formation on Ceo2 and Its Role in the Oxidation of Carbon-Monoxide. *J Chem Soc Chem Comm* **1992,** (14), 977-978.

27.   Nolan, M.; Parker, S. C.; Watson, G. W., The electronic structure of oxygen vacancy defects at the low index surfaces of ceria. *Surf Sci* **2005,** *595* (1-3), 223-232.

28.   Wu, Z. L.; Li, M. J.; Overbury, S. H., On the structure dependence of CO oxidation over CeO2 nanocrystals with well-defined surface planes. *J Catal* **2012,** *285* (1), 61-73.

29.   Liu, X. W.; Zhou, K. B.; Wang, L.; Wang, B. Y.; Li, Y. D., Oxygen Vacancy Clusters Promoting Reducibility and Activity of Ceria Nanorods. *J Am Chem Soc* **2009,** *131* (9), 3140-+.

30.   Vile, G.; Colussi, S.; Krumeich, F.; Trovarelli, A.; Perez-Ramirez, J., Opposite Face Sensitivity of CeO2 in Hydrogenation and Oxidation Catalysis. *Angewandte Chemie-International Edition* **2014,** *53* (45), 12069-12072.

31.   Tang, W.-X.; Gao, P.-X., Nanostructured cerium oxide: preparation, characterization, and application in energy and environmental catalysis. *MRS Communications* **2016,** *6* (4), 311-329.

32.   (a) Yu, J. C.; Zhang, L. Z.; Lin, J., Direct sonochemical preparation of high-surface-area nanoporous ceria and ceria-zirconia solid solutions. *J Colloid Interf Sci* **2003,** *260* (1), 240-243; (b) Barreca, D.; Gasparotto, A.; Maccato, C.; Maragno, C.; Tondello, E., Toward the innovative synthesis of columnar CeO2 nanostructures. *Langmuir* **2006,** *22* (21), 8639-8641; (c) He, Y. J.; Yang, B. L.; Cheng, G. X., On the oxidative coupling of methane with carbon dioxide over CeO2/ZnO nanocatalysts. *Catal Today* **2004,** *98* (4), 595-600; (d) Inguanta, R.; Piazza, S.; Sunseri, C., Template electrosynthesis of CeO2 nanotubes. *Nanotechnology* **2007,** *18* (48); (e) Wang, S. F.; Gu, F.; Li, C. Z.; Cao, H. M., Shape-controlled synthesis of CeOHCO3 and CeO2 microstructures. *J Cryst Growth* **2007,** *307* (2), 386-394; (f) Hosokawa, S.; Shimamura, K.; Inoue, M., Solvothermal synthesis of ceria nanoparticles with large surface areas. *Mater Res Bull* **2011,** *46* (11), 1928-1932; (g) Yu, K. L.; Ruan, G. L.; Ben, Y. H.; Zou, J. J., Convenient synthesis of CeO2 nanotubesl. *Mat Sci Eng B-Solid* **2007,** *139* (2-3), 197-200; (h) Wu, G. S.; Xie, T.; Yuan, X. Y.; Cheng, B. C.; Zhan, L. D., An improved sol-gel template synthetic route to large-scale CeO2 nanowires. *Mater Res Bull* **2004,** *39* (7-8), 1023-1028.

33.   Wu, N. C.; Shi, E. W.; Zheng, Y. Q.; Li, W. J., Effect of pH of medium on hydrothermal synthesis of nanocrystalline cerium (IV) oxide powders. *J Am Ceram Soc* **2002,** *85* (10), 2462-2468.

34.   Wu, Z. L.; Li, M. J.; Howe, J.; Meyer, H. M.; Overbury, S. H., Probing Defect Sites on CeO2 Nanocrystals with Well-Defined Surface Planes by Raman Spectroscopy and O-2 Adsorption. *Langmuir* **2010,** *26* (21), 16595-16606.

35.   Zhu, F. Y.; Wang, Q. Q.; Zhang, X. S.; Hu, W.; Zhao, X.; Zhang, H. X. In *3D reconstruction and feature extraction for analysis of nanostructures by SEM imaging*, 2013 Transducers & Eurosensors XXVII: The 17th International Conference on Solid-State Sensors, Actuators and Microsystems (TRANSDUCERS & EUROSENSORS XXVII), 16-20 June 2013; 2013; pp 2700-2703.

36.   Seiler, H., Secondary electron emission in the scanning electron microscope. *J Appl Phys* **1983,** *54* (11), R1-R18.

37.   (a) Bumbrah, G. S.; Sharma, R. M., Raman spectroscopy – Basic principle, instrumentation and selected applications for the characterization of drugs of abuse. *Egyptian Journal of Forensic Sciences* **2016,** *6* (3), 209-215; (b) Dietzek, B.; Cialla, D.; Schmitt, M.; Popp, J., Introduction to the Fundamentals of Raman Spectroscopy. *Springer Ser Opt Sci* **2010,** *158*, 21-42.

38.   (a) WACHS, I. E.; HARDCASTLE, F. D., Applications of Raman spectroscopy to heterogeneous catalysis. *Catalysis* **1993,** *10*, 102-153; (b) Stencel, J. M., Raman spectroscopy for catalysis. **1989;** (c) Wachs, I. E., Raman and IR studies of surface metal oxide species on oxide supports: supported metal oxide catalysts. *Catal Today* **1996,** *27* (3-4), 437-455; (d) Bartlett, J.; Cooney, R., Raman spectroscopic studies in chemisorption and catalysis. *Advances in spectroscopy* **1987,** *14*, 187-283.

39.   (a) Wachs, I. E., Raman Spectroscopy of Catalysts, in Handbook of Spectroscopy. 2001; (b) Daniel, M.; Loridant, S., Probing reoxidation sites by in situ Raman spectroscopy: differences between reduced CeO2 and Pt/CeO2. *J Raman Spectrosc* **2012,** *43* (9), 1312-1319.

40.   Chalmers, J. M.; Edwards, H. G.; Hargreaves, M. D., *Infrared and Raman spectroscopy in forensic science*. John Wiley & Sons: 2012.

41.   (a) Mestl, G., In situ Raman spectroscopy for the characterization of MoVW mixed oxide catalysts. *J Raman Spectrosc* **2002,** *33* (5), 333-347; (b) Weckhuysen, B. M., Snapshots of a working catalyst: possibilities and limitations of in situ spectroscopy in the field of heterogeneous catalysis. *Chem Commun* **2002,** (2), 97-110; (c) Kuba, S.; Knozinger, H., Time-resolved in situ Raman spectroscopy of working catalysts: sulfated and tungstated zirconia. *J Raman Spectrosc* **2002,** *33* (5), 325-332.

42.   Tuller, H., Mixed conduction in nonstoichiometric oxides. *Nonstoichiometric oxides* **1981**, 271-335.

43.   Ko¨rner, R.; Ricken, M.; No¨lting, J.; Riess, I., Phase transformations in reduced ceria: Determination by thermal expansion measurements. *J Solid State Chem* **1989,** *78* (1), 136-147.

44.   Faber, J.; Seitz, M. A.; Mueller, M. H., Defect characterization in CeO2–x at elevated temperatures—II: Neutron diffraction. *Journal of Physics and Chemistry of Solids* **1976,** *37* (10), 909-915.

45.   (a) Weber, W. H.; Hass, K. C.; Mcbride, J. R., Raman-Study of Ceo2 - 2nd-Order Scattering, Lattice-Dynamics, and Particle-Size Effects. *Phys Rev B* **1993,** *48* (1), 178-185; (b) Nakajima, A.; Yoshihara, A.; Ishigame, M., Defect-Induced Raman-Spectra in Doped Ceo2. *Phys Rev B* **1994,** *50* (18), 13297-13307; (c) Rives, V.; Kannan, S., Layered double hydroxides with the hydrotalcite-type structure containing Cu2+, Ni2+ and Al3+. *J Mater Chem* **2000,** *10* (2), 489-495; (d) Sánchez Escribano, V.; Fernández López, E.; Panizza, M.; Resini, C.; Gallardo Amores, J. M.; Busca, G., Characterization of cubic ceria–zirconia powders by X-ray diffraction and vibrational and electronic spectroscopy. *Solid State Sci* **2003,** *5* (10), 1369-1376.

46.   (a) Taniguchi, T.; Watanabe, T.; Sugiyama, N.; Subramani, A. K.; Wagata, H.; Matsushita, N.; Yoshimura, M., Identifying Defects in Ceria-Based Nanocrystals by UV Resonance Raman Spectroscopy. *J Phys Chem C* **2009,** *113* (46), 19789-19793; (b) Livneh, T.; Sterer, E., Effect of pressure on the resonant multiphonon Raman scattering in UO2. *Phys Rev B* **2006,** *73* (8).

47.   Mcbride, J. R.; Hass, K. C.; Poindexter, B. D.; Weber, W. H., Raman and X-Ray Studies of Ce1-Xrexo2-Y, Where Re=La, Pr, Nd, Eu, Gd, and Tb. *J Appl Phys* **1994,** *76* (4), 2435-2441.

48.   (a) Mamontov, E.; Egami, T., Structural defects in a nano-scale powder of CeO 2 studied by pulsed neutron diffraction. *Journal of Physics and Chemistry of Solids* **2000,** *61* (8), 1345-1356; (b) Mamontov, E.; Egami, T.; Brezny, R.; Koranne, M.; Tyagi, S., Lattice defects and oxygen storage capacity of nanocrystalline ceria and ceria-zirconia. *The Journal of Physical Chemistry B* **2000,** *104* (47), 11110-11116.

49.   (a) Yarwood, J.; Douthwaite, R.; Duckett, S., Spectroscopic Properties of Inorganic and Organometallic Compounds Techniques, Materials and Applications Volume 45 Preface. *Spec Per Rep Spectro* **2014,** *45*, Vii-Vii; (b) Binet, C.; Daturi, M.; Lavalley, J. C., IR study of polycrystalline ceria properties in oxidised and reduced states. *Catal Today* **1999,** *50* (2), 207-225.

50.   Zhao, Y.; Teng, B. T.; Wen, X. D.; Zhao, Y.; Chen, Q. P.; Zhao, L. H.; Luo, M. F., Superoxide and Peroxide Species on CeO2(111), and Their Oxidation Roles. *J Phys Chem C* **2012,** *116* (30), 15986-15991.

51.   (a) Choi, Y. M.; Abernathy, H.; Chen, H. T.; Lin, M. C.; Liu, M., Characterization of O2-CeO2 interactions using in situ Raman spectroscopy and first-principle calculations. *Chemphyschem* **2006,** *7* (9), 1957-63; (b) Pushkarev, V. V.; Kovalchuk, V. I.; d'Itri, J. L., Probing defect sites on the CeO2 surface with dioxygen. *J Phys Chem B* **2004,** *108* (17), 5341-5348.

52.   Kovalenko, M. A.; Kupryazhkin, A. Y., Isotopic effect at oxygen diffusion in imperfect crystals of cerium oxide. *Tech Phys+* **2015,** *60* (2), 155-161.

53.   (a) de Carolis, S.; Pascual, J. L.; Pettersson, L. G. M.; Baudin, M.; Wojcik, M.; Hermansson, K.; Palmqvist, A. E. C.; Muhammed, M., Structure and electronic properties of Ca-doped CeO2 and implications on catalytic activity: An experimental and theoretical study. *J Phys Chem B* **1999,** *103* (36), 7627-7636; (b) Liu, W.; Flytzani-Stephanopoulos, M., Reduction of SO₂ to Elemental S over Ceria Catalysts. In *Environmental Catalysis*, American Chemical Society: 1994; Vol. 552, pp 375-392.

54.   (a) Yoshimura, Y.; Kijima, N.; Hayakawa, T.; Murata, K.; Suzuki, K.; Mizukami, F.; Matano, K.; Konishi, T.; Oikawa, T.; Saito, M., Catalytic cracking of naphtha to light olefins. *Catalysis Surveys from Japan* **2001,** *4* (2), 157-167; (b) Chen, J. Q.; Bozzano, A.; Glover, B.; Fuglerud, T.; Kvisle, S., Recent advancements in ethylene and propylene production using the UOP/Hydro MTO process. *Catal Today* **2005,** *106* (1), 103-107; (c) Bhasin, M.; McCain, J.; Vora, B.; Imai, T.; Pujado, P., Dehydrogenation and oxydehydrogenation of paraffins to olefins. *Applied Catalysis A: General* **2001,** *221* (1), 397-419; (d) Harding, R.; Peters, A.; Nee, J., New developments in FCC catalyst technology. *Applied Catalysis A: General* **2001,** *221* (1), 389-396.

55.   Sheldon, R. A.; Downing, R. S., Heterogeneous catalytic transformations for environmentally friendly production. *Applied Catalysis A: General* **1999,** *189* (2), 163-183.

56.   Haber, J., Fifty years of my romance with vanadium oxide catalysts. *Catal Today* **2009,** *142* (3–4), 100-113.

57.   Lopez, J. M.; Gilbank, A. L.; Garcia, T.; Solsona, B.; Agouram, S.; Torrente-Murciano, L., The prevalence of surface oxygen vacancies over the mobility of bulk oxygen in nanostructured ceria for the total toluene oxidation. *Appl Catal B-Environ* **2015,** *174*, 403-412.